# Monte Carlo study of the effects of system geometry and antiscatter grids on cone-beam CT scatter distributions

A. Sisniega
*Department of Biomedical Engineering, Johns Hopkins University, Baltimore, Maryland 21205 and Departamento de Bioingeniería e Ingeniería Aeroespacial, Universidad Carlos III, ES-28911 Madrid, Spain*

W. Zbijewski[a)]
*Department of Biomedical Engineering, Johns Hopkins University, Baltimore, Maryland 21205*

A. Badal and I. S. Kyprianou
*Division of Imaging and Applied Mathematics, OSEL, CDRH, U.S. Food and Drug Administration, Silver Spring, Maryland 20993-0002*

J. W. Stayman
*Department of Biomedical Engineering, Johns Hopkins University, Baltimore, Maryland 21205*

J. J. Vaquero
*Departamento de Bioingeniería e Ingeniería Aeroespacial, Universidad Carlos III, ES-28911 Madrid, Spain*

J. H. Siewerdsen
*Department of Biomedical Engineering, Johns Hopkins University, Baltimore, Maryland 21205; Department of Computer Science, Johns Hopkins University, Baltimore Maryland 21287; and Russell H. Morgan Department of Radiology, Johns Hopkins University, Baltimore Maryland 21205*

(Received 19 October 2012; revised 8 March 2013; accepted for publication 24 March 2013; published 25 April 2013)

**Purpose:** The proliferation of cone-beam CT (CBCT) has created interest in performance optimization, with x-ray scatter identified among the main limitations to image quality. CBCT often contends with elevated scatter, but the wide variety of imaging geometry in different CBCT configurations suggests that not all configurations are affected to the same extent. Graphics processing unit (GPU) accelerated Monte Carlo (MC) simulations are employed over a range of imaging geometries to elucidate the factors governing scatter characteristics, efficacy of antiscatter grids, guide system design, and augment development of scatter correction.

**Methods:** A MC x-ray simulator implemented on GPU was accelerated by inclusion of variance reduction techniques (interaction splitting, forced scattering, and forced detection) and extended to include x-ray spectra and analytical models of antiscatter grids and flat-panel detectors. The simulator was applied to small animal (SA), musculoskeletal (MSK) extremity, otolaryngology (Head), breast, interventional C-arm, and on-board (kilovoltage) linear accelerator (Linac) imaging, with an axis-to-detector distance (ADD) of 5, 12, 22, 32, 60, and 50 cm, respectively. Each configuration was modeled with and without an antiscatter grid and with (i) an elliptical cylinder varying 70–280 mm in major axis; and (ii) digital murine and anthropomorphic models. The effects of scatter were evaluated in terms of the angular distribution of scatter incident upon the detector, scatter-to-primary ratio (SPR), artifact magnitude, contrast, contrast-to-noise ratio (CNR), and visual assessment.

**Results:** Variance reduction yielded improvements in MC simulation efficiency ranging from ~17-fold (for SA CBCT) to ~35-fold (for Head and C-arm), with the most significant acceleration due to interaction splitting (~6 to ~10-fold increase in efficiency). The benefit of a more extended geometry was evident by virtue of a larger air gap—e.g., for a 16 cm diameter object, the SPR reduced from 1.5 for ADD = 12 cm (MSK geometry) to 1.1 for ADD = 22 cm (Head) and to 0.5 for ADD = 60 cm (C-arm). Grid efficiency was higher for configurations with shorter air gap due to a broader angular distribution of scattered photons—e.g., scatter rejection factor ~0.8 for MSK geometry versus ~0.65 for C-arm. Grids reduced cupping for all configurations but had limited improvement on scatter-induced streaks and resulted in a loss of CNR for the SA, Breast, and C-arm. Relative contribution of forward-directed scatter increased with a grid (e.g., Rayleigh scatter fraction increasing from ~0.15 without a grid to ~0.25 with a grid for the MSK configuration), resulting in scatter distributions with greater spatial variation (the form of which depended on grid orientation).

**Conclusions:** A fast MC simulator combining GPU acceleration with variance reduction provided a systematic examination of a range of CBCT configurations in relation to scatter, highlighting the magnitude and spatial uniformity of individual scatter components, illustrating tradeoffs in CNR and artifacts and identifying the system geometries for which grids are more beneficial (e.g., MSK) from those in which an extended geometry is the better defense (e.g., C-arm head imaging). Compact

geometries with an antiscatter grid challenge assumptions of slowly varying scatter distributions due to increased contribution of Rayleigh scatter. © *2013 American Association of Physicists in Medicine*. [http://dx.doi.org/10.1118/1.4801895]

Key words: cone-beam CT, x-ray scatter, antiscatter grid, image quality, Monte Carlo, GPU

## I. INTRODUCTION

Recent years have seen a proliferation of cone-beam CT (CBCT) in a diversity of preclinical and clinical embodiments and a range of application-specific configurations and geometries, including systems for small animal imaging,[1,2] musculoskeletal extremity imaging,[3,4] otolaryngology imaging,[5–7] breast imaging,[8,9] intraoperative imaging on mobile or fixed-room C-arms,[10–12] and image-guided radiation therapy on a medical linear accelerator.[13,14] Optimization of CBCT imaging performance has presented an area of vigorous research, with x-ray scatter commonly identified as one of the key physical factors limiting image quality. Specifically, x-ray scatter is recognized to impart a loss in contrast, a decrease in contrast-to-noise ratio, loss in detective quantum efficiency (DQE), a loss of spatial resolution, and an increase in cupping and streak artifacts.[15–19] Consequently, considerable effort has been devoted to measuring the magnitude and influence of scatter in CBCT, minimizing x-ray scatter within a particular configuration (e.g., optimizing the air gap and/or using antiscatter grids), and modeling scatter distributions for purposes of scatter correction.

Physical methods of characterizing x-ray scatter in CBCT often involve measurement of signal in the shadow of an x-ray opaque "blocker" placed between the source and the object such that the signal behind the blocker is mainly due to scatter, and the unblocked signal arises from scatter + primary. Such blockers include arrays of small beam stoppers covering the projection field of view (FOV),[20–23] the x-ray beam collimators themselves,[24] a semiopaque blocker pattern to modulate x-ray scatter in a manner that can be decomposed by Fourier methods,[25] and a converse approach in which a beam pass array[26] transmits narrow pencil beams for estimation of primary signal.

Similarly, analytical models of scatter have formed an area of considerable interest. The simplest form assumes a constant scatter fluence in each projection over the entire scan[16] or in individual projections.[27] A somewhat more sophisticated approach assumes the scatter to be a low-pass-filtered version of the primary signal,[28,29] modeling the x-ray beam as a field of pencil beams in which scatter is estimated as a superposition of each beam convolved with the scatter point spread function (kernel) governed by the object thickness. Such scatter kernels can be measured or simulated using Monte Carlo (MC) methods.[30,31]

Monte Carlo simulation offers a potentially accurate method for scatter estimation, but has been somewhat limited in application due to high computational complexity associated with the large number of photon histories (order $\sim 10^9$) needed to produce scatter estimates with an acceptably low level of noise.[32] Encouraging methods for MC acceleration are obtained from so-called variance reduction techniques, known from the general theory of MC simulation in terms of forced detection, mean free path transformations, Woodcock tracking, interaction splitting, and Russian roulette. When appropriately implemented, such techniques can yield ~10–100× reduction in simulation time needed to achieve a given noise level.[33] Another class of acceleration techniques exploits the relative smoothness of x-ray scatter distributions, estimating scatter from a coarse CBCT volume with relatively few photon histories and only a subset of projections followed by filtering and/or interpolation to arrive at low-noise scatter estimates for the full scan.[34–38] Further acceleration can potentially be obtained by modeling 1st-order scatter (single-scatter events) using an analytical model and employing a coarse MC simulation to estimate a smooth background of higher-order scatter.[39] Finally, MC simulation can be significantly accelerated by implementation on graphics processing units (GPUs) that provide a fast, parallel computing architecture with standard desktop workstations. The work reported below was performed using a GPU-accelerated MC implementation based on publicly available software library (MC-GPU) recently reported to offer a 27-fold speedup in simulation time over a single CPU.[40]

CBCT system design for a particular application and development of optimal scatter correction methods stand to benefit from: (i) understanding the nature and form of x-ray scatter components (i.e., incoherent, coherent, and multiple scatter) contributing to the total scatter; (ii) the extent to which scatter rejection with antiscatter grids benefits image quality; and (iii) the effect of system geometry (e.g., source-to-object and object-to-detector distance) on the magnitude, nature, and spatial distribution of x-ray scatter and its components. Neitzel[41] provided an insightful analytical treatment of the question of system geometry (relative to antiscatter grids) in limiting x-ray scatter, concluding generally that systems with a short object-to-detector distance (i.e., a small "air gap") benefit most from use of an antiscatter grid, whereas systems that can accommodate a large air gap (i.e., a large object-to-detector distance) benefit foremost from the extended geometry in rejecting x-ray scatter, and a grid may be of little use (or actually detrimental, due to absorption of primary) to overall image quality per unit dose. Factors such as FOV, electronic noise, focal spot blur, and—of course—limitations in scanner size suitable to a given application present important additional considerations in system geometry, but the relationship between scatter and system geometry is known to be a particularly steep function of "selectivity"—e.g., scatter fluence varying by more than an order of magnitude over the range of geometries relevant in clinical CBCT.

Interestingly, the diversity of preclinical and clinical CBCT configurations in various applications spans a full

range of such system geometries, with some featuring a compact form with a small air gap and others involving an extended geometry with a large air gap. This diversity of geometries, along with the associated variety of imaging techniques and object size implies that the susceptibility to scatter is not the same for all CBCT embodiments. This point is reflected in recent studies on the effects of x-ray scatter in such contexts. In a particular small animal CBCT geometry, for example, Colijn *et al.*[42] showed scatter-to-primary ratios (SPR) of 10%–20% for rat-sized objects. In musculoskeletal extremity imaging, Zbijewski *et al.*[3] found ~20% scatter-induced cupping and showed that antiscatter grids significantly reduce such artifact and improve contrast-to-noise ratio (CNR) without increase in imaging dose. In breast imaging, Kwan *et al.*[43] measured ~50% SPR at the detector for an average-size breast (14 cm diameter) and showed the benefit of a bowtie filter in reducing scatter. For mobile C-arm imaging, Schafer *et al.*[44] showed that an antiscatter grid did not offer an improvement in CNR per unit square root dose. Similarly, Kyriakou *et al.*[45] found that for low- to medium-scatter levels in C-arm CT, an increase in x-ray exposure was needed to compensate for primary absorption in the grid. In kilovoltage (kV) CBCT for image-guided radiotherapy (IGRT), Siewerdsen *et al.*[46] showed that although grids significantly reduced cupping and streak artifacts, image uniformity, and CT number accuracy, they did not offer an improvement in CNR per unit square root dose and offered little or no qualitative improvement in soft-tissue visibility (prostate). Similarly, Lazos and Williamson[47] used MC simulations to show that antiscatter grids in CBCT for IGRT gave little or no improvement in CNR for head and neck imaging and a 10%–20% improvement in CNR for pelvic imaging at a fixed dose.

Such work paints a spectrum of system geometry and distinct considerations of x-ray scatter relevant to new CBCT imaging systems. Furthermore, not only does system geometry govern the magnitude of x-ray scatter, it also governs the form of the x-ray scatter—i.e., the relative contribution of incoherent and coherent scatter components within the total scatter fluence and the spatial distribution of these components at the detector. The relative contribution of such components can be important in x-ray scatter correction—e.g., some methods assuming scatter to present a slowly varying (low frequency) spatial distribution with little or no structure.[24,27]

The work reported below was motivated by this general backdrop of x-ray scatter within a broad diversity of CBCT scanner embodiments and applications. As detailed below, we leverage a modified form of the MC-GPU simulation software across a spectrum of system geometries to investigate not only the magnitude of x-ray scatter within each configuration but also the relative components (incoherent, coherent, and multiple scatter) therein. The work also sheds light on the potential merits (or detriments) of antiscatter grids within various system geometries, the influence of grid orientation on scatter rejection, and the spatial distribution of scatter at the detector—in some configurations found to be far from slowly varying. The work is not intended as a specific form of x-ray scatter correction (although the MC-GPU simulation could certainly be incorporated in a scatter correction framework); rather, the work is intended to describe the effect of system geometry and antiscatter grids on the magnitude, form, and spatial distribution of x-ray scatter across a range of pertinent CBCT applications in broad terms that will identify key considerations in understanding the performance of current embodiments, designing new systems, and developing x-ray scatter correction methods.

## II. MATERIALS AND METHODS

### II.A. GPU-accelerated Monte Carlo simulation platform

The simulation engine was based on the MC-GPU v1.1 package,[40] which exploits the capacity for parallel computing in modern GPUs for efficient implementation of MC x-ray photon tracking in a voxelized object geometry. The MC-GPU package is explained in detail in Ref. 40 and is publicly available via the U. S. Food and Drug Administration, Center for Devices and Radiological Health (http://code.google.com/p/mcgpu/). The code employs interaction models and cross sections from PENELOPE 2006,[48] a general-purpose MC simulation system for electron-photon transport, and achieves a 15- to 30-fold acceleration over computation on a single CPU.

#### *II.A.1. Polyenergetic x-ray source model*

Tungsten anode x-ray spectra with arbitrary filtration were obtained from the Spektr toolkit[49] implementation of the TASMIP polynomial model.[50] The spectra were provided to MC-GPU as a text file with 1 keV sampling intervals over the range 1–150 keV. The x-ray spectra were normalized to yield a probability density function, and the energy of each photon was determined using sampling by Walker's alias method.[51]

#### *II.A.2. Photon tracking and variance reduction techniques*

MC-GPU tracks individual x-ray photons through the voxelized volume using Woodcock tracking.[52] The length of the step between interactions is calculated assuming a uniform object composed of the most attenuating material in the volume. Some interactions are then treated as virtual (i.e., not resulting in a change to photon energy or trajectory), depending on the material encountered at the interaction site. With this approach, explicit computation of photon path intersections with each voxel boundary is avoided, yielding algorithmic acceleration and execution speeds independent of voxel size. Photon histories with the (weighted) energy falling below 5 keV are terminated. To further increase the speed in simulating x-ray scatter distributions, we implemented the following additional variance reduction techniques in the MC-GPU engine.

*II.A.2.a. Forced scattering.* All nonvirtual interactions were forced to be either Compton or Rayleigh scatter by eliminating photoelectric absorption from the set of possible

interactions and adjusting the photon weight to correct for the resulting bias:

$$w_i = w_{i-1}\frac{\mu_c + \mu_r}{\mu_t}, \quad (1)$$

where $w_i$ is the weight after interaction $i$, $w_{i-1}$ is the weight carried by the photon from previous interactions, $\mu_c$ and $\mu_r$ are the Compton and Rayleigh components of the attenuation coefficient, respectively, and $\mu_t$ is the total attenuation coefficient for the voxel at which the interaction occurs.

*II.A.2.b. Interaction splitting and forced detection.* Upon selecting the interaction type, the photon was split into several ($N_{\text{split}}$) virtual photons, each of them with a weight reduced by $1/N_{\text{split}}$ from that of the original photon.[33] For Compton scatter interactions, the direction of each virtual photon was forced toward a randomly selected detector pixel, thus assuring detection.[53,54] (Forcing toward all pixels would be prohibitively slow due to the large number of elements in the detector matrix). A weight was assigned to the photon to correct for the bias resulting from neglecting other possible directions:[45]

$$w_i = w_{i-1}\sigma_c^{-1}\frac{d\sigma_c}{d\Omega}\Delta\Omega, \quad (2)$$

where $\sigma_c$ is the total Compton scattering cross section, $d\sigma_c/d\Omega$ is the differential Compton cross section for the direction from the interaction site to the center of the detector pixel, and $\Delta\Omega$ is the solid angle covered by the detector pixel. The differential cross section was computed by PENELOPE with the Klein-Nishina formula corrected for electron binding effects using the impulse approximation.[48] The expression (2) is approximate, since the differential cross section is assumed constant across a detector pixel. For small pixels (e.g., <1 mm for flat-panel detectors), the change in scattering angle across a pixel is small and thus the error is expected to be negligible; no appreciable bias was found in scatter distributions obtained with forced detection compared to standard simulation (see Sec. III.A). The resulting virtual scattered photon was advanced toward the detector using Woodcock tracking, allowing only for virtual interactions, but weighting the photon contribution by the probability of interaction every time the transport function is sampled (and thus accounting for attenuation along the photon track). Photon splitting was also performed for Rayleigh interactions, but forced detection was not employed, since it did not significantly improve simulation speed (i.e., most photons undergoing Rayleigh scatter advanced toward the detector anyway). After an initial scattering event (and scoring the resulting virtual photon in the detector), the simulation proceeded to model multiple scatter by returning to track the original photon in the usual manner to the next scatter event, scoring the resulting virtual photon in the detector, and so on until the photon traversed the object.

Interaction splitting can be detrimental to overall performance of a parallel MC implementation in that it breaks the continuity of each primary photon thread when the virtual scattered photons are created and advanced toward the detector. The tracking process was therefore modified to optimize for parallel execution of interaction splitting on a GPU. Primary photons originating from the x-ray source were tracked in parallel until all of them reached their first interaction points. Subsequently, the status of the primary photons was stored in GPU memory and the threads associated with tracking them were terminated. A new group of threads was created for each original photon to undergo virtual interactions and to track the virtual photons to the detector in a fully parallel fashion. After all the virtual photons reached the detector, their threads were terminated and a new set of kernels was launched to continue the tracking of the original photons from their saved state.

*II.A.2.c. Ray-tracing of primary signal.* For a given number of simulated photons, the variance reduction techniques described above decrease noise in the simulated scatter distributions but have no effect on the noise in the simulated primary signal. When variance reduction is applied to accelerate MC simulation by lowering the number of tracked photons, the noise in the resulting primary estimates reflects this reduced photon fluence and may therefore be relatively large. Instead of relying on MC simulations of the primary, a GPU implementation of a polychromatic Siddon ray-tracer[55] employing the same spectrum, system geometry, and material properties as the MC engine was therefore separately executed to yield a noiseless estimate of the primary signal. Complete projections (primary + scatter) were computed by adding the primary and scatter signals after correction by their respective simulated gain (air) projections.

### *II.A.3. Analytical model for the antiscatter grid and flat-panel detector*

Transmission through a focused antiscatter grid and interaction of x-ray photons in the detector scintillator were modeled deterministically by applying analytical weights to each photon reaching the detector plane. The grid was approximated as locally parallel, oblique lamellae oriented at an angle corresponding to the angle of the focused grid at the location of photon incidence. Each photon was assigned a weight given by the analytical expression of Day and Dance[47,56] for grid transmission as a function of photon incidence angle, photon energy, grid cell materials and dimensions, and local grid angle. The photon was subsequently scored in the detector with a weight representing the product of energy-dependent probability of absorption in the scintillator (quantum detection efficiency, $\overline{g_1}$), and energy-dependent optical gain in the scintillator ($\overline{g_2}$). For a flat-panel detector with a 250 mg/cm$^2$ CsI:Tl scintillator, the mean detector response has been accurately modeled in these terms by cascaded systems analysis,[57] with $\overline{g_1}$ computed from the incident x-ray spectrum and attenuation coefficient of CsI, and $\overline{g_2}$ assuming a gain of 50 photons per keV absorbed.[58] Typically, the detection process as modeled by cascaded systems analysis also includes gain stages to account for escape efficiency of optical photons from the scintillator ($\overline{g_3}$), and coupling efficiency of the scintillator and photodiodes ($\overline{g_4}$), and pixel fill factor. Since those gains are nearly independent of photon energy and therefore cancel out in gain correction (air-scan normalization), they have no impact on the analysis of scatter distributions below and were modeled as additional

TABLE I. Nominal geometry and phantoms for the various CBCT configurations.

| CBCT configuration | X-ray spectrum | SAD (mm) | ADD (mm) | Mag | *D* (mm) | *d* (mm) | Common phantom Major axis (mm) | Realistic phantom | |
|---|---|---|---|---|---|---|---|---|---|
| | | | | | | | | Anatomy type | Major axis (mm) |
| Small animal (SA) | 60 kVp (1 mm Al) | 150 | 50 | 1.3 | 150 | 0.293 | 70 | Rat | 52 |
| Extremity (MSK) | 90 kVp (0.2 mm Cu, 2 mm Al) | 430 | 120 | 1.3 | 250 | 0.488 | 160 | Knee | 125 |
| Head | 90 kVp (0.2 mm Cu, 2 mm Al) | 480 | 220 | 1.5 | 250 | 0.488 | 160 | Head | 235 |
| Breast | 80 kVp (0.2 mm Cu, 2 mm Al) | 458 | 320 | 1.7 | 300 | 0.586 | 140 | Breast | 140 |
| C-arm | 100 kVp (0.2 mm Cu, 2 mm Al) | 600 | 600 | 2.0 | 430 | 0.840 | 160 | Head and thorax | 235 and 500 (incl. arms) |
| Linac | 110 kVp (0.2 mm Cu, 2 mm Al) | 1000 | 500 | 1.5 | 430 | 0.840 | 280 | Thorax and pelvis | 500 (incl. arms) and 350 |

empirical weight factors applied to the photon when scored in the detector. The weight was chosen to yield signal levels that agreed with the measured mean detector response for a Varian 4030CB flat-panel detector within ~5%–10% for spectra ranging 60–150 kVp.

### II.B. CBCT system and object models

To elucidate the geometric factors governing the magnitude of x-ray scatter and the individual components therein (viz., Compton and Rayleigh), a pertinent range of CBCT configurations currently deployed in clinical and preclinical applications was considered: (1) a small animal scanner[2] (denoted SA); (2) a compact musculoskeletal extremities scanner[3] (denoted MSK); (3) an otolaryngology head scanner (denoted Head);[7] (4) a dedicated breast scanner[59](denoted Breast); (5) a mobile intraoperative C-arm[12] (denoted C-arm); and (6) a kV CBCT imager implemented on a linear accelerator[46](denoted Linac). The geometries approximating such configurations are summarized in Table I and Fig. 1. Systems were defined by their source-to-axis distance (SAD), axis-to-detector distance (ADD), and detector size (*D*, the lateral and longitudinal extent of the flat-panel detector). In each case, the flat-panel detector format was taken as a 512 × 512 matrix of square pixels at pitch *d* in combination with a 250 mg/cm$^2$ CsI:Tl scintillator. The x-ray beam extended laterally (fan angle) and longitudinally (cone angle) to match the detector area. The configurations illustrated in Fig. 1 were not intended to model any particular, commercially available system and instead reflect fairly generic CBCT geometries appropriate to a given application. The flat-panel detector was centered on the central axis of the x-ray beam in each case, and "offset-detector" geometries were not considered. A bowtie filter was not incorporated in the current work since many of the systems considered do not commonly employ a bowtie. There is therefore no simple, nominal choice of filter for each configuration that would permit a fair comparison across this range of geometry, object size, and kVp. Rather, the design of bowtie filters optimal to a particular configuration is a continuing area of work, with results indicating potential advantages in x-ray scatter for some configurations (e.g., breast CT[43] and Linac CBCT[47,60]). For simplicity in an already broad space of parameters considered below, the simulations considered scenarios without a bowtie.

Each configuration was considered with and without an antiscatter grid. The focal distance of the grid was equal to the source-detector distance (SDD) in each case. Simulations were performed with grid lamellae nominally oriented perpendicular to the axis of rotation (denoted "grid horizontal") and alternatively oriented with lamellae parallel to the axis of rotation (denoted "grid vertical"). Again to limit an already broad scope of parameters, a single nominal grid design was considered in all simulations—specifically, a 10:1 grid ratio, 200 lines per in. (7.87 lines per mm), focused linear grid comprising Pb lamellae with Al interspacers. This model represents an intermediate grid of fairly standard design, thus providing a common basis for comparisons. Potentially more beneficial grid designs (e.g., air interspacers, variable lines per inch, 2D crosshatch, etc.), and optimal choice of grid parameters for the particular system geometry were beyond the scope of the current work. Previous work also showed that the

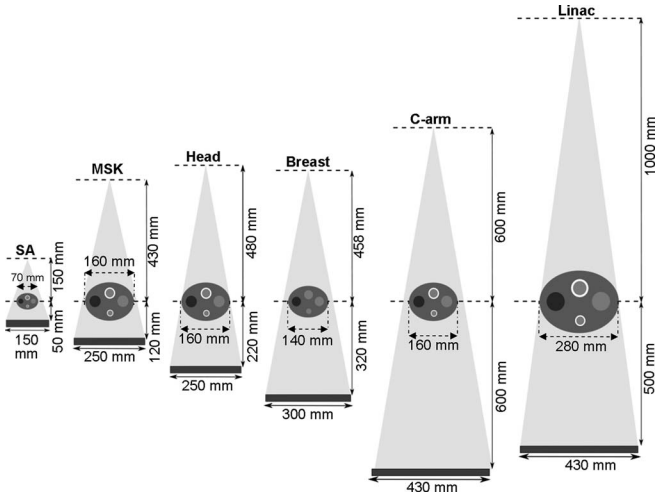


FIG. 1. Geometric configurations illustrated to scale with the common elliptical phantom.

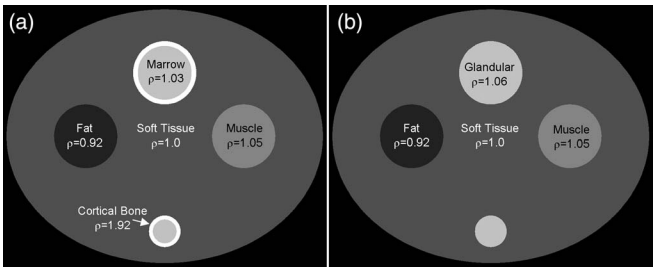


FIG. 2. (a) Illustration of the idealized Common Phantom as used in the simulations of the SA, MSK, Head, C-arm, and Linac CBCT. For the Breast configuration (b), the bone inserts were replaced by glandular tissue.

particular grid design (e.g., grid ratio) had only a fairly weak effect on scatter effects, and a nominal (10:1 grid ratio) was a reasonable choice. Nevertheless, the results below can be used to provide guidance for system-specific grid design by identifying key aspects of scatter distribution and grid performance for each embodiment.

The digital phantoms comprised various combinations of the following materials: air, lung, adipose, soft tissue, brain, skin, muscle, cartilage, red marrow, and cortical bone. The interaction cross sections for each material were computed from the elemental composition data obtained either from the PENELOPE database[48] (soft tissue and fat) or from the tabulated data by Woodard and White.[61] Two categories of digital phantom were considered: (1) a generic elliptical phantom referred to as the "Common Phantom" providing a common basis of comparison among each of the CBCT configurations; and (2) a set of anatomically realistic phantoms ranging from mouse to human pelvis as detailed below.

An axial slice of the Common Phantom is illustrated in Fig. 2. The background region consisted of soft tissue, and a pair of low contrast (muscle and fat) inserts was included along the major axis. Two bone inserts were included along the minor axis, comprising an annulus of cortical bone around a marrow interior. For the breast configuration, the two bone regions were replaced by glandular tissue. The size of the Common Phantom was scaled between each of the CBCT configurations as detailed in Table I to represent approximately the size of anatomy in each application (without lateral truncation), maintaining a constant ratio of the minor to major axes of 0.8. The phantom extended longitudinally (to infinite length) beyond the longitudinal FOV. The voxel size for the Common Phantom was chosen to minimize discretization artifacts in Siddon ray-tracing of primary x-rays: 0.03 mm for the SA configuration, 0.07 mm for the Breast, 0.08 mm for the MSK, Head, and C-arm, and 0.15 mm for the Linac.

A variety of anatomically realistic phantoms were also simulated as listed in Table I. For the SA configuration, the Digimouse[62] model was scaled to simulate a rat thorax with voxel size 0.29 mm. For the MSK, Head, C-arm, and Linac configurations, anthropomorphic models of a knee, a head, a thorax, and a pelvis were built from models included in the Virtual Family Project[63,64] dataset at voxel size 1.0 mm. For the Breast configuration, a digital breast phantom was constructed from a manually segmented breast CBCT volume[65] of a breast at voxel size 0.5 mm. Materials in the realistic phantoms included air, lung, adipose, soft tissue, brain, skin, muscle, cartilage, red marrow, and cortical bone, with cross sections computed from the same resources as described above for the Common Phantom. For all models, the original discretization of the source datasets was maintained.

## II.C. Monte Carlo experiments

### *II.C.1. Validation of Monte Carlo variance reduction techniques*

Validation of the basic MC-GPU package in comparison to measurements and an established, CPU-based MC implementation (PENELOPE) has been previously reported in the context of dose scoring.[66,67] The MC variance reduction techniques (forced scattering, photon splitting, and forced detection) in our implementation of MC-GPU were further validated by computing scatter distributions with and without variance reduction for a variety of CBCT configurations using the Common Phantom and a 70 kVp (+2 mm Al, +0.2 mm Cu added filtration) x-ray spectrum. The simulations were performed ten times in each case with the number of photon histories per projection ($N_{\text{ph}}$) ranging from $5 \times 10^6$ to $5 \times 10^8$. An additional MC-GPU simulation obtained with $10^{10}$ photons/projection and no variance reduction provided a reference standard against which to assess possible bias introduced by the acceleration techniques. The performance of MC simulation at a given number of photon histories was quantified using the following efficiency figure of merit:

$$\varepsilon = \sum_i \left( \frac{\bar{x}_i}{\sigma_i} \right)^2 \frac{1}{\bar{t}}, \tag{3}$$

where $\sigma_i$ is the standard deviation of pixel $i$, $\overline{x_i}$ is the mean value for pixel $i$, and $\bar{t}$ is the average execution time of the MC simulation, all computed over ten independent MC runs. The variance reduction techniques should yield lower noise for a given number of simulated photons compared to simulations without such acceleration, but at the cost of potential increase in run-time. The ratio ($R_\varepsilon$) of $\varepsilon$ with and without variance reduction therefore assessed the performance gain.

### *II.C.2. Effects of system geometry on scatter: Continuously varied SAD and SDD*

An initial set of simulations systematically varied the system geometry across a broad range beyond the specific CBCT configurations of Fig. 1 to provide a more general understanding of the effects of system geometry on scatter fractions and grid efficacy. The SAD was varied from 10 to 130 cm, and the SDD was varied from 60 to 150 cm (each in ~5 cm increments, such that the former was always less than the latter). The Common Phantom was used in each case (with major axis set to 16 cm), and a single projection perpendicular to the major axis was simulated. The number of histories was $N_{\text{ph}} = 5 \times 10^6$ photons, split into 512 virtual photons at each interaction. Since the spatial distribution of scatter was not analyzed in this case, only a small centrally located detector region of 20 × 20 pixels was used for scoring and subsequent

computation of average SPR. All Compton photons were forced toward the detector, allowing for further reduction of simulation noise. Simulations were performed with and without an antiscatter grid using a 100 kVp (+2 mm Al, +0.2 mm Cu added filtration) spectrum and a detector of size $D = 250$ mm. For simulations with a grid, the focal length was equal to the SDD.

#### II.C.3. Specific CBCT configurations: Scatter distributions, image artifacts, and efficacy of an antiscatter grid

The main body of experiments involved analysis and comparison of scatter properties and grid efficacy for the CBCT configurations summarized in Table I and Fig. 1. In each case, scatter and primary projections were simulated for both the Common Phantom and the realistic anatomical models using the nominal parameters in Table I, with and without the antiscatter grid. Simulations were performed for a complete circular orbit of projections at 1° angular steps, and scatter estimation involved $N_{\text{ph}} = 5 \times 10^6$ photons per projection split into 512 virtual photons at each interaction. While the noise in scatter distributions obtained with variance reduction for this $N_{\text{ph}}$ is low (see Sec. III.A), additional denoising of the scatter fluence was performed by executing three iterations of a Richardson-Lucy (RL) fit with a Gaussian kernel,[34,36] with a kernel width of 10 pixels for Compton and multiple scatter distributions and 4 pixels for Rayleigh scatter distributions. This approach has been shown to reduce simulation noise without biasing the distributions.[34] RL fitting was used to denoise the scatter distributions in the studies of various CBCT system configurations but was not used in the validation study (Sec. II.C.1) or the basic study of system geometry (Sec. II.C.2). Noiseless primary x-ray projections were computed with the Siddon algorithm and added to the total scatter distribution after a normalization of both distributions by their respective gain (air) scans. The same antiscatter grid was employed for primary and scatter simulations, as detailed in Sec. II.B. The simulated projections (scatter + primary) were reconstructed with the Feldkamp algorithm[68] on a 256 × 256 × 40 isotropic voxel grid with a Hann apodizer with a cutoff at the Nyquist frequency. The reconstruction voxel size varied between the configurations so that the side of the cubic reconstruction volume was always 110% of the major axis of the Common Phantom for that embodiment: 0.29 mm for the SA configuration, 0.69 mm for the MSK, Head, and C-arm, 0.6 mm for the Breast, and 1.21 mm for the Linac.

### II.D. Metrics of scatter assessment

The magnitude of the total scatter and Compton and Rayleigh components therein was quantified in terms of the gain-corrected scatter magnitude ($S_{\text{tot}}$), the gain-corrected magnitude of each scatter component [Compton ($S_{\text{incoh}}$), Rayleigh ($S_{\text{coh}}$), and multiple scatter ($S_{\text{multi}}$)], the fraction of each component in the total scatter signal, and the scatter-to-primary ratio (SPR). The deflection angle was measured for each scattered photon reaching the detector as the angle between the direction of travel and the line connecting the focal spot with the point of interaction with the detector. Thus a deflection angle of 0° indicated travel direction parallel to the lamellae of a focused grid. For the experiments with the Common Phantom, the metrics are reported as means measured from a 20 × 20 pixel region of interest (ROI) located at the center of the detector, and the deflection angle was analyzed as an angular histogram over the same ROI weighted by the weight of each photon and normalized to unity total area. For the realistic phantoms, box plots were used to represent the distribution of metrics in the region of the projected shadow of the object. The degradation of image quality associated with x-ray scatter was evaluated by the following quantitative metrics as well as visual inspection of the reconstructed images:

#### II.D.1. Cupping

Taking $\mu_{\text{center}}$ and $\mu_{\text{edge}}$ as the mean value of a 20 × 20 voxel ROI at the center and inside edge of the object, respectively, the magnitude of cupping artifact was assessed as

$$t_{\text{cup}} = 100 \times \frac{\mu_{\text{edge}} - \mu_{\text{center}}}{\mu_{\text{edge}}}. \quad (4)$$

#### II.D.2. Contrast reduction

Soft-tissue contrast between muscle and fat in reconstructions of the Common Phantom was computed as

$$C = 2\frac{\mu_M - \mu_F}{\mu_M + \mu_F}, \quad (5)$$

where $\mu_M$ and $\mu_F$ are the mean values of a 20 × 20 voxel ROI inside the muscle and fat inserts, respectively. The reduction in contrast due to scatter was quantified by the ratio of contrast in a reconstruction of the complete simulated projection data (including primary and scatter, $C_{\text{prim+scat}}$) to that in a reconstruction of primary-only projections ($C_{\text{prim}}$). Contrast and cupping were computed for the Common Phantom, where the regular elliptical shape and placement of inserts yielded a symmetric cupping pattern with respect to the major axes, and streak artifacts were localized and well separated from the muscle and fat inserts. This provided a reliable estimate of contrast from Eq. (5) without potential bias introduced by the placement of ROIs relative to a complicated pattern of artifacts in the more realistic anatomical phantoms.

#### II.D.3. Contrast-to-noise ratio

The scatter and primary projections obtained by MC simulation with variance reduction do not realistically convey the quantum noise in a projection image at a given level of radiation dose. However, consideration of image noise is important when assessing the performance of antiscatter grids because of the reduction of primary fluence and the associated increase in noise due to attenuation in the grid. We therefore used an analytical model to analyze the relative change in contrast-to-noise ratio (CNR, including both the improvement in contrast and the increase in noise) associated with the introduction of a grid as a function of SPR. Denoting the transmission of

primary photons by the grid as $g_{\text{prim}}$ and the transmission of scattered photons as $g_{\text{scat}}$, the SPR in the presence of the grid is

$$\text{SPR}_{\text{grid}} = \left(\frac{g_{\text{scat}}}{g_{\text{prim}}}\right) \text{SPR}_{\text{no-grid}}. \quad (6)$$

As derived in Ref. 69 for a circular insert of attenuation $\mu_1$ and diameter $d_1$ inside a uniform circular region of diameter $d_0$ and attenuation coefficient $\mu_0$, the contrast (difference in mean measured voxel values between $\mu_0$ and $\mu_1$) in the presence of scatter is

$$C = \delta + \frac{1}{d_1} \ln\left(\frac{1 + \text{SPR}e^{-\delta d_1}}{1 + \text{SPR}}\right), \quad (7)$$

where $\delta = \mu_0 - \mu_1$ is the intrinsic material contrast (i.e., difference in true attenuation coefficient). Although Eq. (7) shows addition of a term to the intrinsic material contrast $\delta$, the SPR-dependent natural logarithm term always has opposite sign to that of $\delta$, and scatter always results in a reduction in the difference between reconstructed voxel values. Ignoring electronic noise, the pixel variance in the reconstructed image $N^2$ is inversely proportional to the detected x-ray intensity.[70] Assuming the same tube output (mAs) for image acquisition with and without the grid, and denoting the intensities of primary and scatter radiation on the detector as $I^{\text{prim}}$ and $I^{\text{scat}}$, the ratio of the (squared) CNR at a fixed dose with and without a grid is

$$\begin{aligned}
\frac{\text{CNR}^2_{\text{grid}}}{\text{CNR}^2_{\text{no-grid}}} &= \left(\frac{C_{\text{grid}}/N_{\text{grid}}}{C_{\text{no-grid}}/N_{\text{no-grid}}}\right)^2 \\
&= \frac{\left(I^{\text{prim}}_{\text{grid}} + I^{\text{scat}}_{\text{grid}}\right)}{\left(I^{\text{prim}}_{\text{no-grid}} + I^{\text{scat}}_{\text{no-grid}}\right)} \left(\frac{C_{\text{grid}}}{C_{\text{no-grid}}}\right)^2 \\
&= \frac{I^{\text{prim}}_{\text{grid}}(1 + \text{SPR}_{\text{grid}})}{I^{\text{prim}}_{\text{no-grid}}(1 + \text{SPR}_{\text{no-grid}})} \left(\frac{C_{\text{grid}}}{C_{\text{no-grid}}}\right)^2 \\
&= \frac{g_{\text{prim}}(1 + \text{SPR}_{\text{grid}})}{(1 + \text{SPR}_{\text{no-grid}})} \\
&\quad \cdot \frac{\left[\delta + \frac{1}{d_1} \ln\left(\frac{1 + \text{SPR}_{\text{grid}}e^{-\delta d_1}}{1 + \text{SPR}_{\text{grid}}}\right)\right]^2}{\left[\delta + \frac{1}{d_1} \ln\left(\frac{1 + \text{SPR}_{\text{no-grid}}e^{-\delta d_1}}{1 + \text{SPR}_{\text{no-grid}}}\right)\right]^2}. \quad (8)
\end{aligned}$$

The dependence of the ratio of CNR with and without the grid in Eq. (8) on SPR was computed for each of the CBCT configurations for a setup approximating the Common Phantom, taking $\mu_0$ for soft tissue (computed at the effective beam energy, equal to spectrum-weighted mean energy) and with $d_0$ matching the major axis. The attenuation coefficient and diameter of the insert ($\mu_1$ and $d_1$) was taken as the muscle insert (Fig. 2). Grid transmission factors $g_{\text{prim}}$ and $g_{\text{scat}}$ were obtained for each CBCT embodiment from MC simulations of Sec. II.C.3 by averaging over a 20 × 20 pixel ROI at the center of the detector. Note that the derivations of Eqs. (7) and (8) assume that the introduction of the contrast insert ($d_1$, $\mu_1$) into the background object ($d_0$, $\mu_0$) introduces only a small perturbation that does not influence SPR or the measured value of the background attenuation in the presence of scatter. It is also assumed that scatter carries no information and acts purely as an uncorrelated (i.e., equal noise-power at all spatial frequencies) additive source of projection noise as detailed in Ref. 69.

## III. RESULTS

### III.A. Validation of variance reduction techniques

Figure 3 shows example results of the scatter fluence computed for the Linac CBCT geometry. The magnitude of simulated scatter depends on the total number of photon histories, much as it depends on x-ray fluence in real systems. To facilitate direct comparison but avoid modifications to the shape of the distributions caused by air normalization, the scatter projections were rescaled to $10^8$ photon histories. The total scatter distribution obtained with the variance reduction techniques [i.e., forced scattering, interaction splitting and forced detection in Fig. 3(a), denoted Variance Red. ON] was significantly less noisy (pixel signal-to-noise ratio averaged over the detector $\bar{x}/\sigma = 11.81$ for the Linac geometry considered in Fig. 3) than the distribution obtained without variance reduction [Fig. 3(b), denoted Variance Red. OFF, $\bar{x}/\sigma = 1.98$] with comparable computation time even though the former used only ~1/20 as many photon histories [$N_{\text{ph}} = 5 \times 10^6$ in Fig. 3(a) versus $10^8$ in Fig. 3(b)]. As expected, signal-to-noise ratio was proportional to the square root of the run time for unaccelerated MC-GPU. When the number of photon histories in unaccelerated MC-GPU was increased by another factor of 100, the signal-to-noise improved by a factor of 10 [Fig. 3(c), Variance Red. OFF, $\bar{x}/\sigma = 19.76$]. Consequently, the ~6× increase in signal-to-noise ratio achieved with variance reduction at equal run time corresponds to ~40× shorter run time than unaccelerated MC-GPU at equal signal-to-noise ratio. Figure 3(d) shows the absolute relative difference image of the Variance Red. ON distribution [Fig. 3(a)] and the "gold standard" Variance Red. OFF distribution obtained with $10^{10}$ photon histories [Fig. 3(c)]. The low mean value (~2.6%) and uniformity of the distribution of the relative difference indicate that the variance reduction techniques did not introduce bias (i.e., shift or distortion) in the simulated scatter distributions.

The results demonstrate that inclusion of forced scattering, photon splitting, and forced detection in MC-GPU yielded improved signal-to-noise ratio at shorter execution times. The efficiency improvement [Eq. (3)] achieved with variance reduction is quantified in Table II. Introduction of interaction splitting provided the most substantial increase in simulation efficiency over MC-GPU with no variance reduction, ranging from $R_\varepsilon$ ~6 for breast CBCT to $R_\varepsilon$ ~10 for other configurations. This improvement in efficiency was achieved despite the modified tracking process that incurs additional computation time due to switching between the kernels tracking the original and virtual photons at every interaction, as described in Sec. II.A.2. A comparatively small gain from splitting is found for breast CBCT, since Woodcock tracking treats the step length between interactions as the mean free path of the most attenuating material in the sample. The mean free path

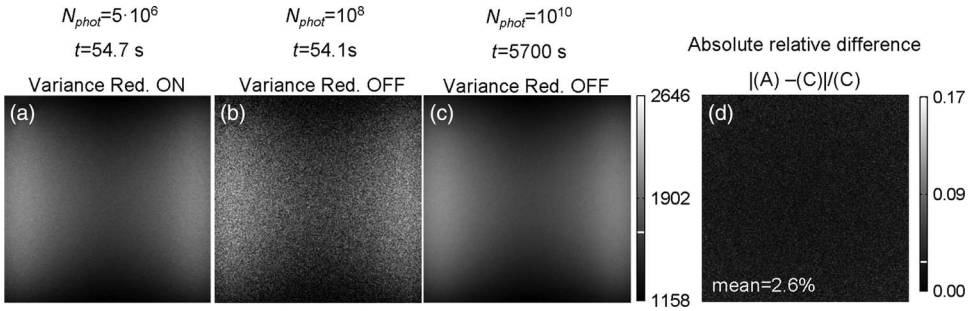


FIG. 3. Total scatter distributions computed with and without variance reduction techniques for the Linac geometry. (a) MC-GPU with variance reduction (Variance Red. ON) with $5 \times 10^6$ photon histories. (b) MC-GPU with no variance reduction (Variance Red. OFF) and $10^8$ photon histories. (c) "Gold standard" MC-GPU without variance reduction and $10^{10}$ photon histories. (d) The relative difference image computed between the distribution obtained with variance reduction (a) and the "gold standard" distribution (c). In each case, the white bar on the colorbar indicates the mean of the respective distributions.

of glandular tissue is larger than that of bone (the most attenuating material in the Common Phantom for all configurations except the breast), so the simulation for breast CBCT involves fewer virtual interactions between real interactions than other configurations. The relative increase in the simulation time due to switching the tracking kernels in interaction splitting is therefore larger for breast than other configurations. Inclusion of forced detection and forced scattering in addition to interaction splitting yielded additional ~2-fold improvement in efficiency for SA and MSK, and ~3-fold improvement in efficiency for other configurations. This additional gain is predominantly due to forced detection. The use of forced scattering for configurations employed in this study resulted in a decrease in $R_\varepsilon$ ranging from 15% for SA to 25% for Linac. The performance of forced scatter depends however on the average number of interactions encountered by a photon prior to leaving the object or being terminated at an energy threshold and on the relative probability of absorption compared to scatter. A 20% improvement in efficiency over MC-GPU was found for breast CBCT with a 45 keV (+1 mm Al) spectrum (significantly softer than the nominal beam used here). Because forced scattering offered this potential benefit for some configurations, particularly at lower energies, it was incorporated among the MC-GPU variance reduction techniques used throughout this study. The total gain with all three variance reduction techniques is smallest for SA ($R_\varepsilon \sim 20$) and largest for C-arm and Head CBCT ($R_\varepsilon \sim 35$).

### III.B. Effects of system geometry on scatter: Continuously varied SAD and SDD

Figure 4 quantifies a number of important, general dependencies between x-ray scatter, system geometry, and the relative benefit of an antiscatter grid. Figure 4(a) plots the SPR at the center of the detector over a broad range of possible CBCT geometries for the Common Phantom fixed at a major axis diameter of 16 cm and a projection perpendicular to the major axis of the phantom. The steep reduction in SPR for higher ADD is clear, consistent with trends noted by Neitzel[41] and others[45,71] that increasing the air gap is the first best defense against x-ray scatter. For compact geometries (e.g., those with ADD ~8–30 cm) in particular, the variation of SPR with ADD is dramatic (note logarithmic scale) such that small increases in air gap yield strong reduction in SPR. The dependence on SDD is comparatively weak, with only a slight increase in SPR at increased SDD due to a decrease in the deflection angle required for photons that undergo scatter at the object periphery to reach the detector center (where SPR is computed). This decrease in the deflection angle yields increased probability of interactions that contribute to SPR as explained below.

The reduction in SPR achieved with an antiscatter grid is shown in Fig. 4(b). The benefit of grids is greater for compact systems (i.e., those with shorter ADD). As shown in the histogram of deflection angle [Fig. 4(c)], the distribution of the direction of scattered photons reaching the detector is broader for a compact system geometry than for more extended configurations, with the peak of the histogram shifted away from 0° (the direction parallel to the lamellae of a focused grid), resulting in increased scatter rejection by a focused grid. Systems with larger ADD mainly involve forward-directed scatter reaching the detector, so the grid gives less benefit. At a fixed ADD, grids provide less SPR reduction [higher ratio of SPR in Fig. 4(b)] for systems with shorter SDD, since the short SDD implies a steep deflection angle needed for scattered photons generated near the periphery of the object to reach the

TABLE II. MC simulation efficiency ratio ($R_\varepsilon$) for various combinations of variance reduction techniques.

| Variance reduction techniques | SA | MSK | Head | Breast | C-arm | Linac |
|---|---|---|---|---|---|---|
| Standard MC-GPU (Variance Red. OFF) | 1.00 | 1.00 | 1.00 | 1.00 | 1.00 | 1.00 |
| Interaction splitting | 9.25 | 10.69 | 10.33 | 6.23 | 11.04 | 11.06 |
| Interaction splitting + forced detection + forced scatter (Variance Red. ON) | 17.57 | 22.80 | 33.89 | 21.72 | 33.99 | 28.36 |

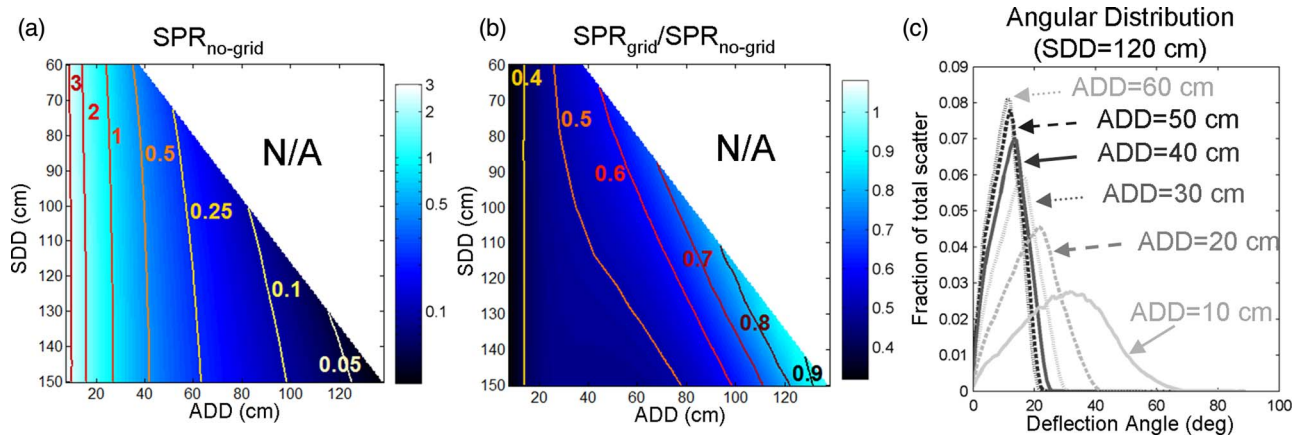


FIG. 4. (a) Scatter-to-primary ratio at the center of the detector versus SDD and ADD for systems without a grid. (b) Reduction in SPR due to an antiscatter grid (10:1 grid ratio). (c) Histogram of deflection angles of scattered photons reaching the detector plane for a projection perpendicular to the major axis of the Common Phantom.

center of the detector. For both coherent and incoherent scatter, the probability of interaction is generally lower for steeper deflection angles. Therefore, compared to a configuration with long SDD, the scatter at the center of the detector for a system with short SDD contains a higher fraction of forward-directed photons that are difficult to remove by a grid.

### III.C. Scatter in various CBCT configurations: Cupping, streaks, contrast, and CNR

Figure 5 shows reconstructions of the Common Phantom across CBCT embodiments for three simulation scenarios: (i) simulation of primary photons only (providing baseline image quality for a polyenergetic x-ray beam); (ii) simulation of primary and scatter photons with no antiscatter grid; and (iii) primary + scatter photons as in (ii) but with a focused horizontal antiscatter grid. The increase in cupping and streak artifacts is apparent for all configurations when scatter is included in the simulation, particularly for the gridless scenario (ii), but the severity of scatter artifacts is strongly dependent on system geometry. The slight degree of cupping and streaks in the primary-only cases (i) is attributed to beam hardening. The images visually illustrate the effects of geometry and the presence of an antiscatter grid on image uniformity (cupping), streaks, and contrast, each quantified in Fig. 6 and discussed in detail below.

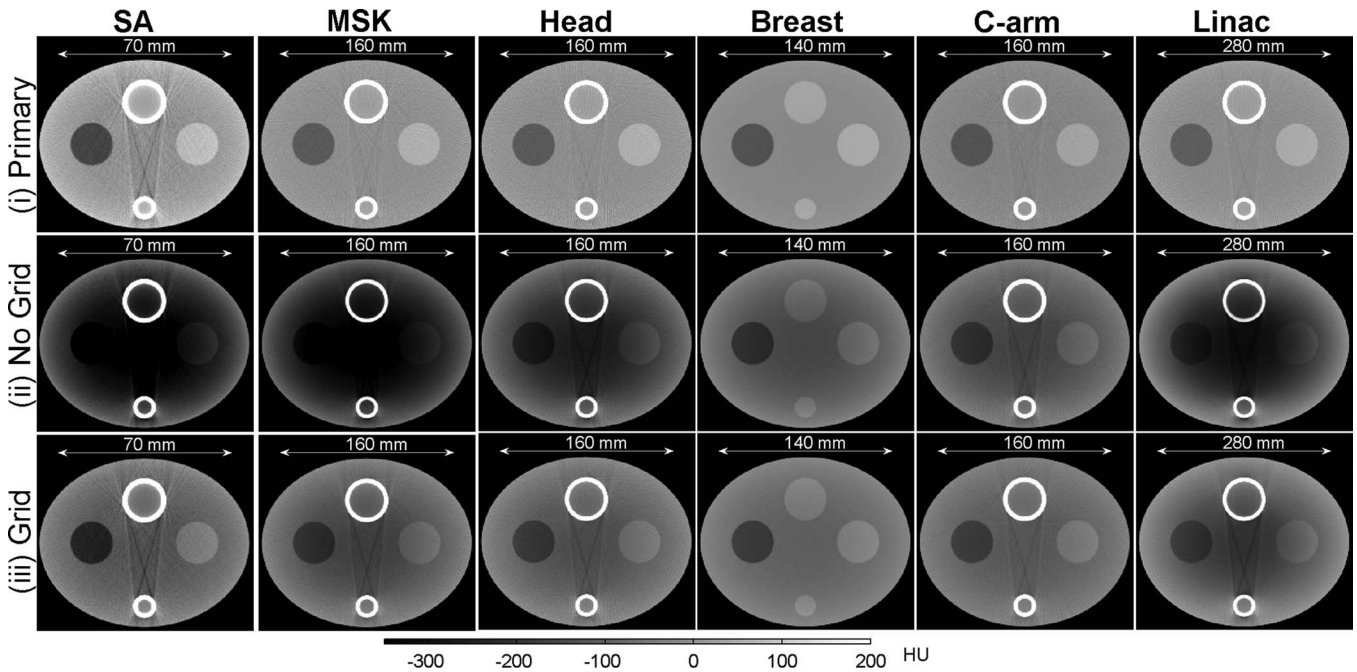


FIG. 5. (i) Axial reconstructions of primary-only projection data for the Common Phantom. (ii) Reconstructions of projections with scatter included in the simulation (without an antiscatter grid). (iii) Reconstructions of primary + scatter projection data with an antiscatter grid.

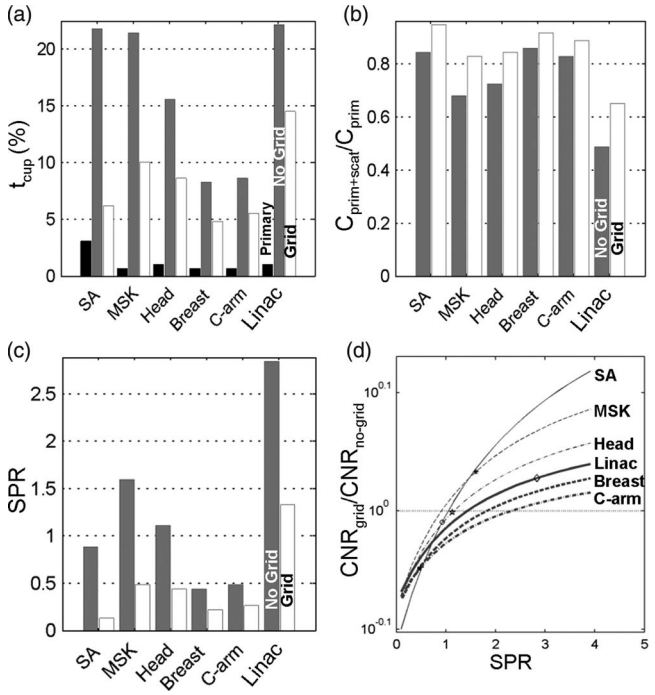


FIG. 6. (a) Cupping artifact [Eq. (4)] in reconstructions of the Common Phantom. (b) Reduction in contrast [from Eq. (5)] in reconstructions of primary + scatter to that in primary-only. (c) SPR in projections of the Common Phantom with and without a grid. Black bars indicate simulations with primary only. Gray bars show simulations with scatter (and no grid). White bars show simulations with scatter and an antiscatter grid. (d) The ratio of CNR with a grid ($CNR_{grid}$) to CNR without a grid ($CNR_{no\text{-}grid}$) plotted versus SPR for each CBCT configuration at fixed detector exposure. The horizontal dotted line marks CNR ratio equal to one.

As illustrated in Fig. 5, cupping is most pronounced for the more compact geometries (such as the MSK and Head scanners) and for large objects (Linac). Figure 6(a) quantifies the increased cupping due to x-ray scatter, where the compact geometries exhibit artifact in the range $t_{cup}$ ~15%–22% (compared to $t_{cup}$ ~1%–3% without scatter). Similarly for the large object (280 mm) Linac case, x-ray scatter increases $t_{cup}$ from ~1% (without scatter) to $t_{cup}$ ~22%. As seen qualitatively in scenario (iii) of Fig. 5, introduction of a grid improves image uniformity (reduces cupping) for all configurations. Consistent with trends suggested in Fig. 4, the most pronounced benefit in image uniformity is for systems with short air gaps (SA and MSK) and large objects (Linac) and less for systems with higher magnification (Breast and C-arm). Figure 6(a) quantifies the major improvement in $t_{cup}$ by virtue of the grid for the SA, MSK, and Head configurations, whereas the improvement for the Breast and C-arm cases is more modest.

Figure 5 also shows that streak artifacts are evident even in the primary-only scenario (i) due to beam hardening (strongest for the SA case, which involves the softest x-ray spectrum) and are intensified in the scatter + primary scenarios. Interestingly, the presence of an antiscatter grid is seen to impart greater benefit to image uniformity (reduced cupping artifact) than to streaks, most evident in the SA, MSK, and Head configurations. This reflects the sensitivity to residual scatter and the ability of grids to reduce slowly varying (low-frequency) scatter artifacts arising from high-angle scatter (Compton and multiple scatter) but lesser ability to reduce high-frequency artifacts associated with low-angle scatter (Rayleigh and, to a lesser degree, low-order Compton).

The loss of contrast due to x-ray scatter is evident in Figs. 5 and 6(b), with greater degradation for the systems exhibiting larger cupping. The recovery of contrast by an antiscatter grid is strongest for the SA, MSK, Head, and Linac configurations and least pronounced for the Breast and C-arm. The diminishing return in the use of grids for configurations with large air gap and medium-sized FOV (i.e., Breast and C-arm) is evident from analysis of the SPR with and without grids in Fig. 6(c), where the SPR at the detector is already a factor of ~2–6 lower than for the other configurations. The results suggest the strongest benefit from the grid for the SA configuration, due not only to the compact geometry but also the soft x-ray spectrum and increased grid efficiency.

Note that the relative magnitude of cupping $t_{cup}$ is not directly related to SPR, as evidenced by a comparison of the SA and Linac cases, which show a similar magnitude of $t_{cup}$, despite a significantly larger SPR for the Linac configuration. This is simply a result of the absolute change in the reconstructed attenuation coefficient depending on SPR and object size[69] (70 mm for SA versus 280 mm for the Linac). The same dependence of reconstructed values on SPR and object size explains the different appearance of reconstructions of the Common Phantom for SA, MSK, and Linac CBCT in Fig. 5, despite similar values of $t_{cup}$. The same $t_{cup}$ can therefore imply a different appearance/severity of the cupping artifact when it is accompanied by different bias in the mean reconstructed attenuation value.

Figure 6(d) shows the relative benefit (or degradation) in CNR associated with an antiscatter grid for each of the CBCT geometries, weighing the increase in contrast obtained by virtue of the grid versus the associated increase in image noise. For each curve in Fig. 6(d), the system geometry is that indicated in Table I, but the SPR was taken as a free variable. [See Fig. 6(c) for the actual SPR at the center of the detector for the posterior-anterior projection of the Common Phantom.] In each case, the ratio of CNR with and without a grid was computed according to the analytical model in Eq. (8) utilizing MC estimates of grid transmission for primary and scatter radiation. A ratio in CNR below 1.0 implies that the grid imparts an increase in noise that outweighs the increase in contrast. For systems with a large air gap and medium-sized objects (e.g., Breast and C-arm), the grid degrades CNR over a broad range of SPR, including those typical of the Common Phantom as plotted in Fig. 6(c). Similarly for the SA configuration, the small object size yields low SPR for which the grid is seen to degrade CNR. For the more compact MSK and Head configurations, the results suggest an improvement in CNR at levels of SPR (~1.0–1.5) typical for those embodiments. The Linac presents an intermediate case, with the large object size leading to high SPR that would favor the use of a grid in terms of CNR, but a fairly long geometry for which the benefits of the grid may be small.

Considering the results of Figs. 5 and 6 in total reveals a mixed set of tradeoffs and considerations for each CBCT

configuration as to whether or not a given system benefits from incorporation of a grid. In all cases, the grid improves image uniformity (reduces cupping), but depending on the SPR may improve or degrade CNR. For the more compact geometries in human applications (MSK and Head) the results are consistent: incorporation of a grid imparts a significant reduction in artifacts and a net benefit to CNR (without increase in dose). For the more extended geometry (Breast and C-arm), the grid has a lesser effect in artifact reduction and reduces CNR. Implications for the SA configuration are mixed: although the grid strongly reduces artifacts, it degrades CNR for the low levels of SPR typical for small subjects even in the compact geometry. Similarly for the Linac, the implications are mixed (but for the opposite reasons): the grid imparts a significant reduction in artifacts but may have little benefit (or in fact, degradation) on CNR, depending on the size of the object, and an increase in dose may be required to restore CNR to that in the gridless configuration. Section IV reviews the consistency of these findings with physical experimentation with and without grids in scanner embodiments comparable to those in Table I.[3,42–47]

### III.D. Scatter in various CBCT configurations: Scatter components and spatial distribution

To gain further understanding of the factors influencing scatter magnitude and grid efficacy, the scatter components (incoherent, coherent, and multiple scatter of any type) are analyzed in Fig. 7 for a single projection perpendicular to the major axis of the Common Phantom. Taking the MSK configuration, for example, the fractions of each component in the total scatter are shown in Fig. 7(a). For this compact geometry, the scatter distribution is dominated by multiple scatter when no grid is present (top row). Introduction of a grid reduces the total scatter, of course, and changes the relative contributions of scatter components. The fraction of multiple scatter is strongly reduced, but there is a nearly twofold increase in the relative contribution of Rayleigh scatter, reflecting lower grid efficiency for forward-directed scattered photons (bottom row). By comparison, the fraction of Compton scatter is not as strongly influenced by the presence of a grid.

Figures 7(b)–7(d) show the contributions of various scatter components more generally versus system geometry (ADD)

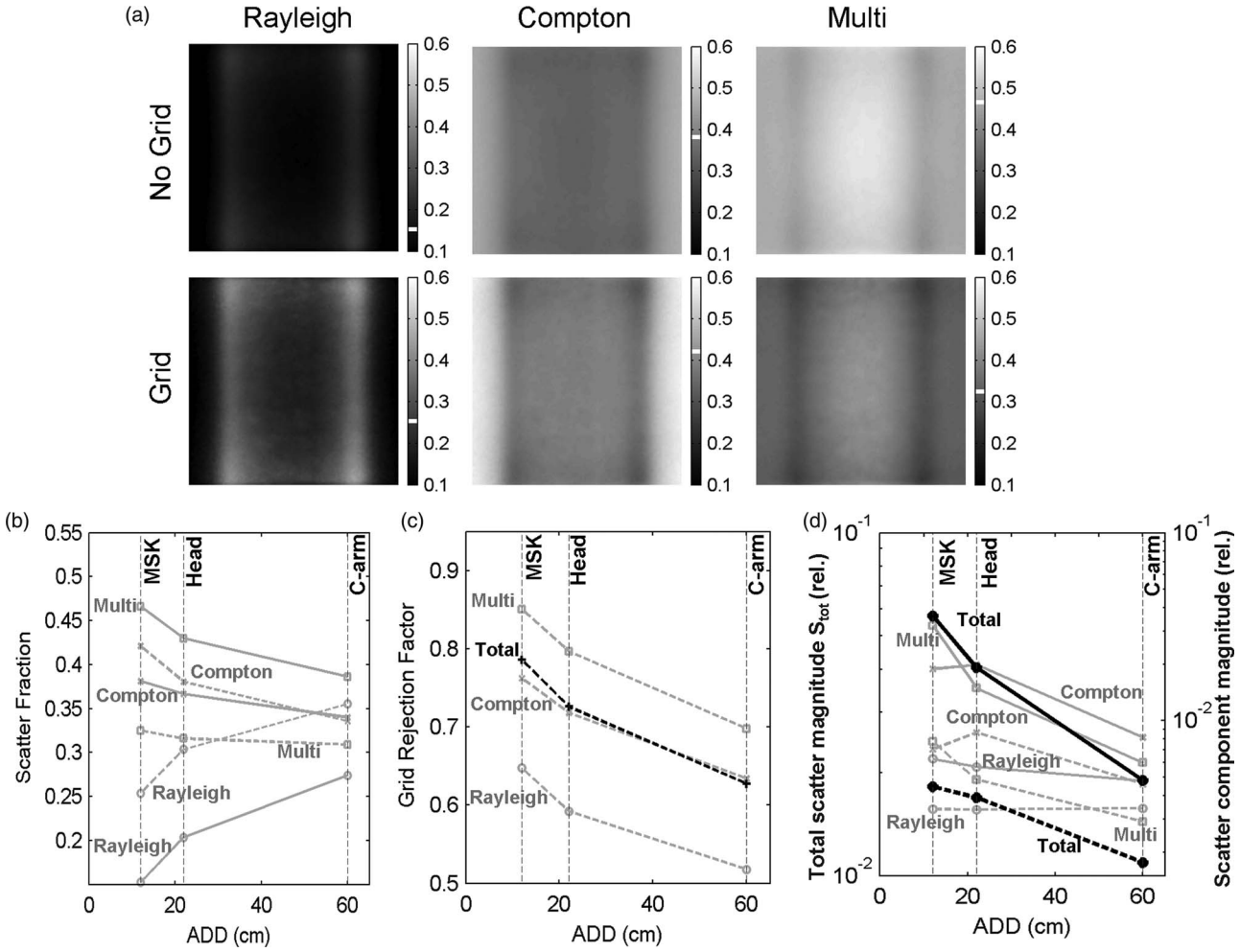


FIG. 7. (a) Distribution (in the plane of the detector) of the fraction of total scatter associated with individual scatter components for MSK CBCT. (b) Fraction of various scatter components versus ADD. (c) Grid rejection factor (i.e., fraction of a given scatter component removed from the total) for each component. (d) Gain-corrected magnitude of total scatter, $S_{tot}$ (left vertical axis) and of all three scatter components $S_{incoh}$, $S_{coh}$, and $S_{multi}$ (right vertical axis). Solid lines: configuration without a grid; dashed lines: configuration with a grid; black lines: total scatter; gray lines: individual scatter components.

showing the MSK, Head, and C-arm configurations specifically for the 16 cm Common Phantom. Figure 7(b) shows that the fraction of each scatter component (Compton, Rayleigh, and multiple) at the center of the detector depends on the scattering angle: Compton and multiple scatter components decrease with longer geometries, but the relative contribution of Rayleigh scatter increases significantly (with or without a grid). Figure 7(c) shows that the efficiency of the grid (i.e., the fraction of a given scatter component rejected) similarly depends on geometry: increasing ADD (i.e., air gap) increases the relative contribution of forward-directed scatter components (i.e., low-angle Compton and Rayleigh scatter) and results in lower grid efficiency for the more extended geometries (e.g., C-arm). Finally, Fig. 7(d) shows the relative contribution of each scatter component by comparing the magnitude of the total scatter (air scan-normalized, to allow comparison in a manner that corrects for inverse-square law) and the three components therein. The magnitude of forward-directed Rayleigh scatter (corrected for inverse-square law) is almost constant across the various CBCT configurations for the fixed 16 cm phantom. The more broad angular distributions of Compton and multiple scatter diminish the amplitude of these scatter components with increasing air gap, and the same is observed for the total scatter.

### III.E. Scatter in various CBCT configurations: Realistic anatomical phantoms

To extend and test the results detailed above for the idealized Common Phantom within a more anatomically realistic context, projections of realistic murine, and anthropomorphic phantoms were simulated for the same CBCT configurations in Table I. Figure 8 shows central axial slices of reconstructions for each phantom and scanner configuration. Overall, we immediately note results consistent with those obtained for the Common Phantom—namely, that both the magnitude of scatter artifacts and the degree of improvement obtained through the incorporation of a horizontal grid are more pronounced for the compact geometries (MSK and Head) and/or large objects (C-arm Thorax and Linac Pelvis). Complex bone anatomy in the realistic phantoms underscores the magnitude of streak artifacts caused by scatter and illustrates the limited ability of grids to reduce such high-frequency artifacts associated with low-angle scatter. Such strong sensitivity to bias caused by residual scatter suggests that applications involving visualization in the vicinity of bone structures would especially benefit from some form of additional scatter correction (e.g., a high-fidelity scatter correction algorithm, perhaps based on MC simulation). The results of Fig. 8 also extend those of Figs. 5–7 in anatomical contexts not approximated by the Common Phantom—viz., the C-arm configuration with a large body site (the Thorax) and the Linac configuration for imaging of a large and more highly attenuating site (the Pelvis)—each with lateral truncation. For the C-arm Thorax, increased scatter fractions are most clearly observable as a loss of quantitative accuracy in the bones compared to imaging a smaller subject as in C-arm Head. In the Linac Pelvis case, streak artifacts and other image nonuniformities are introduced in addition to cupping, despite a smaller fraction of bone in the volume compared to, for example, the head.

Finally, Fig. 9 shows air-scan-normalized primary and total scatter distributions in anterior-posterior (AP) projections of the realistic anatomical phantoms for each CBCT configuration. For each system geometry, the images show that incorporation of a grid reduces the mean intensity of scatter signal, accompanied by an increase in the relative contribution of forward-directed scatter components (i.e., Rayleigh and some single-scatter Compton). For the nominal ("horizontal") grid orientation, spatial distributions of

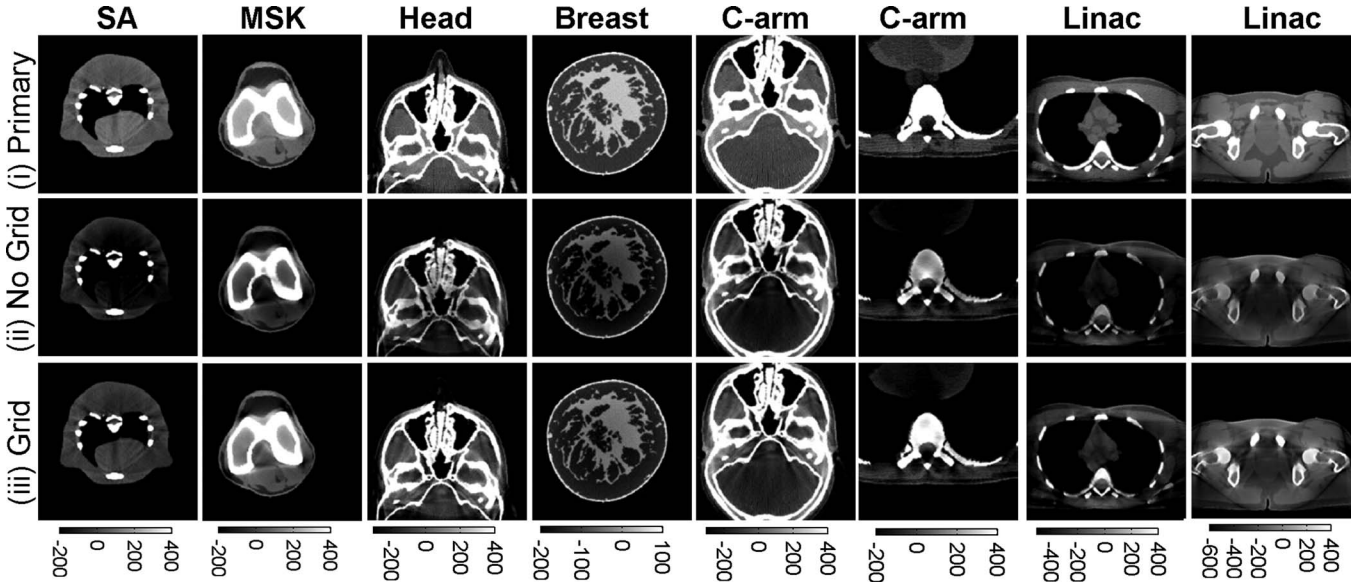


FIG. 8. Axial reconstructions of the anatomical phantoms for the CBCT configurations in Table I. (i) Reconstructions of primary-only projection data. (ii) Reconstructions with scatter included (without an antiscatter grid). (iii) Reconstructions with primary + scatter and an antiscatter grid.

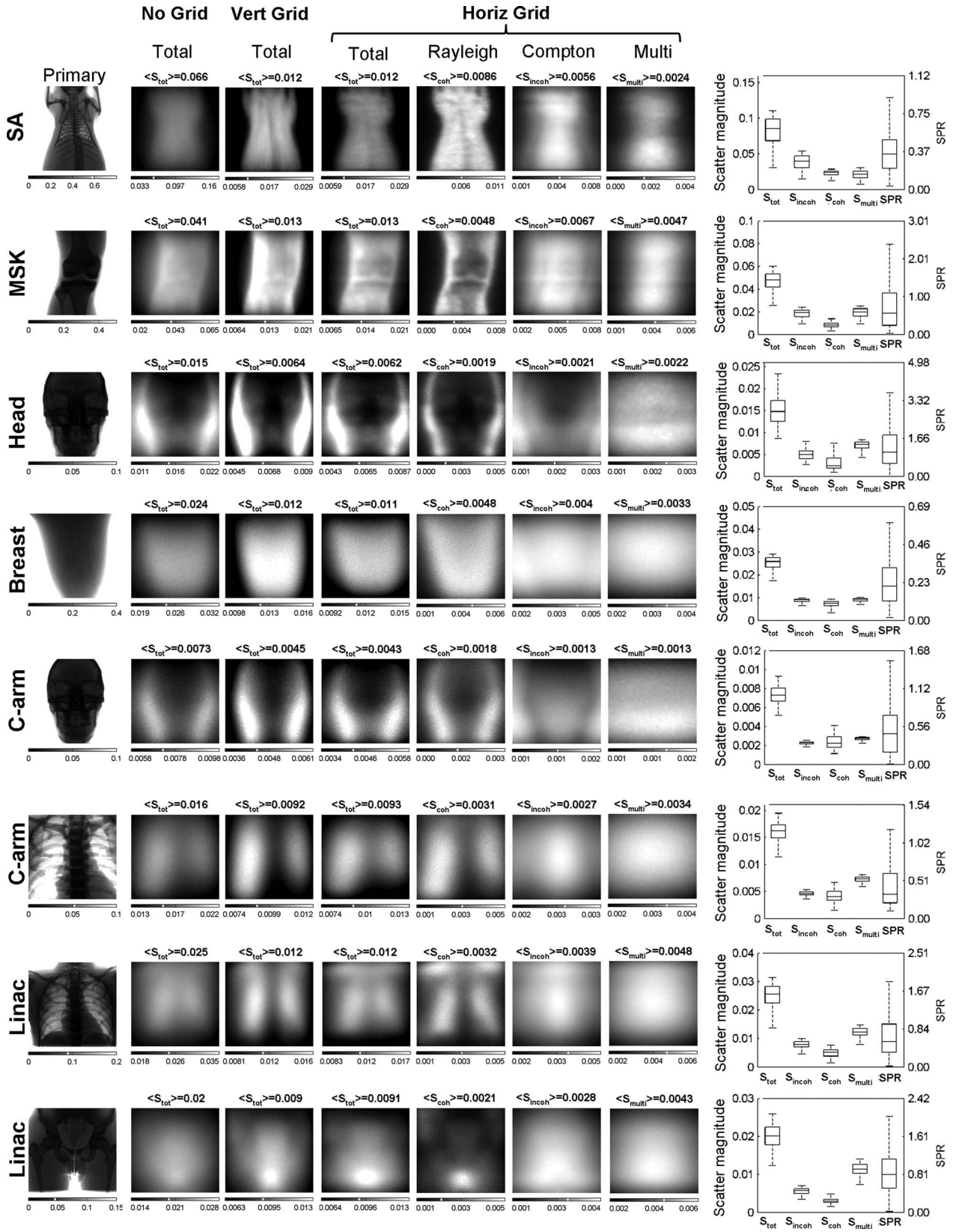


FIG. 9. Distributions of primary, total scatter, and individual scatter components at the detector for various scanner configurations and anatomical sites. Primary and total scatter distributions are shown without and with a grid (both for vertical and horizontal grid orientations). Individual scatter components are shown for the horizontal grid orientation only. The mean total scatter magnitude computed across the detector plane is stated above each distribution. The right column displays the SPR (right vertical axis) and (gain-corrected) intensities of each component (left vertical axis) for gridless configurations.

Rayleigh, Compton, and multiple scatter are shown. Rayleigh scatter distribution exhibits more high-frequency structural information (arising mainly from self-absorption) compared to other scatter components, which tend to present a relatively slowly varying characteristic. The increase in the relative contribution of Rayleigh scatter upon the introduction of a grid therefore results in a scatter distribution exhibiting more pronounced high-frequency structural content. Figure 9 demonstrates that the heterogeneity in the total scatter field in the presence of a grid largely follows that of the coherent scatter distribution. The increase in high-frequency content of both coherent and total scatter distributions is most pronounced for geometries with a shorter air gap (compare, for example, the Head and C-arm cases for the same anthropomorphic head in Fig. 9), reflecting the role of an extended geometry not only in decreasing the magnitude of scatter but also in effectively "blurring" the spatial distribution of scatter by virtue of increased distance from scattering centers.

Figure 9 demonstrates an additional consideration in the orientation of the (linear) antiscatter grid relative to the axis of rotations: "horizontal" (as in all previous results) in which the grid lines are orthogonal to the axis of rotation; and "vertical" in which the grid lines are parallel to the axis of rotation. The particular shape of the resulting scatter distribution depends strongly on grid orientation. The "vertical" grid orientation is aligned parallel to highly attenuating structures in several cases—e.g., the spine (for the SA, C-arm Thorax, and Linac Thorax cases) and the femur or tibia (for the MSK case) and thus preferentially rejects scattered photons generated from outside the shadow of those structures. The vertical grid orientation thus exacerbates the effects of low-angle scatter and self-absorption and results in a scatter distribution with significantly greater high-frequency content compared to the horizontal grid orientation. Incorporation of a grid (and the particular orientation of the grid on the detector) therefore challenges the conventional, often-invoked assumption that x-ray scatter distributions follow a slowly varying (low-frequency) distribution that can be simply modeled as a slowly varying (or constant) function in scatter correction algorithms.

The magnitude of various scatter components and the overall SPR are quantified in the right column of Fig. 9 using box plots summarizing the distributions in the detector plane in the shadow of the object. As hypothesized from the Common Phantom results, the more compact configurations (i.e., shorter air gaps) suffer increased scatter magnitude (all components) and increased relative contributions of Compton and multiple scatter for objects of similar size—illustrated, for example, by comparison of the otolaryngology Head scanner configuration (3rd row of Fig. 9) and the C-arm Head (5th row of Fig. 9), where the former contends not only with higher magnitudes of all scatter components (and total scatter and SPR) but also a greater heterogeneity (high-frequency content) in the scatter distribution. This general trend of reduced scatter with increased air gap is somewhat mitigated by self-absorption in the object: compare again the Head and Breast configurations, where total scatter magnitude is lower for the Head scanner (0.015 vs 0.024, respectively), despite a shorter ADD (220 mm vs 320 mm, respectively). For a fixed geometry (e.g., the C-arm or Linac), the total scatter magnitude, SPR, and fraction of multiple scatter are determined by the volume of the irradiated subject—e.g., comparing the C-arm Head and C-arm Thorax (5th and 6th rows of Fig. 9). Compared to multiple scatter, the fraction of coherent and incoherent scatter appears to be fairly independent of object size for a fixed system geometry, e.g., the ratio $\langle S_{\text{incoh}}\rangle/\langle S_{\text{tot}}\rangle$ changes from 0.30 for C-arm Head to 0.29 for C-arm Thorax, whereas $\langle S_{\text{multi}}\rangle/\langle S_{\text{tot}}\rangle$ changed from 0.36 for C-arm Head to 0.45 for C-arm Thorax. Similarly, for the Linac configuration, $\langle S_{\text{incoh}}\rangle/\langle S_{\text{tot}}\rangle = 0.31$ for the thorax and 0.28 for the pelvis, compared to $\langle S_{\text{multi}}\rangle/\langle S_{\text{tot}}\rangle = 0.49$ for the thorax and 0.56 for pelvis.

## IV. DISCUSSION AND CONCLUSIONS

Inclusion of variance reduction techniques of interaction forcing, photon splitting, and forced detection in MC-GPU yielded a ~6× improvement in the signal-to-noise ratio or a ~40× increase in computation speed over previously reported MC-GPU simulation, which itself involves a ~15–30× increase in speed over calculations performed on a single CPU. Such accelerated MC simulations provide a useful means of examining a broad parameter space of CBCT system design and can potentially form the basis of high-quality scatter correction.[67] Application of this methodology to a systematic study of scatter across a range of clinically relevant CBCT configurations revealed significant effects of system geometry. Compact systems with short ADD (and thus short air gaps), such as small animal, extremities, and otolaryngology CBCT scanners, are dominated by multiple and Compton scatter. A large fraction of scattered photons reaches the detector at oblique angles, enabling effective scatter removal by incorporation of an antiscatter grid. More extended configurations with long ADD (breast, C-arm, and Linac CBCT scanners) have lower scatter magnitudes and exhibit an increased relative contribution of forward directed scatter components, reducing the effectiveness of grids in scatter removal. For a fixed geometry, the contribution of multiple scatter depends on subject size, whereas the relative contributions of Compton and Rayleigh scatter are more affected by geometry than subject size. Grids modify the relative contributions of scatter components and spatial distribution of scatter: forward-directed photons (Rayleigh and single-scatter Compton) are more likely to be transmitted, shifting the spatial distribution toward higher-frequency structure. The orientation of grid lamellae also affects the shape of scatter distributions, which are more uniform for grid lines perpendicular to the dominant orientation of highly attenuating bony structures in the sample—e.g., the femur and tibia in the MSK configuration.

Scatter-induced cupping artifacts can effectively be removed by grids with a concomitant improvement in contrast; both effects are more pronounced for short air gaps and for large irradiated volumes, where grids are generally more efficient. Despite the stronger relative effect of grids (i.e., improvement in contrast and uniformity) for geometries with short air gaps, the absolute magnitude of residual cupping and contrast loss for such configurations is often larger than

or comparable to systems with large air gap without a grid. Analysis of CNR shows moreover that even if grids effectively remove scatter, the CNR at fixed dose can be degraded compared to gridless acquisition due to absorption of primary radiation. Geometries with large air gaps benefit from grids in terms of CNR only for the largest subjects with high SPR. Scatter-induced streak artifacts are not effectively removed by grids, indicating a strong sensitivity to residual bias in the detector signal behind highly attenuating structures and suggesting a need for additional software corrections even in the presence of a grid.

The current study employed a common antiscatter grid of intermediate weight (grid ratio 10:1) and Al interspacers for all CBCT configurations. Other grid designs may offer potential advantages—e.g., air or carbon interspacers giving higher primary transmission, 2D crosshatch designs giving stronger scatter attenuation, or grids with variable grid ratio and/or pitch across the detector designed to increase scatter rejection where it is needed most. The results outlined in this study can help to identify grid parameters that are most likely to yield improved performance for each geometry and thus offer a guide to such optimization. For example, increasing the primary transmission (while maintaining scatter rejection) is likely to yield greater benefit for more extended configurations with a long air gap. For the more compact configurations, a slight reduction in primary transmission (e.g., by increasing the grid ratio) may be acceptable, since the gain in CNR at fixed dose with the standard grid is already high. Furthermore, the broad angular distribution of scattered photons reaching the detector could be exploited to improve scatter rejection by employing 2D focused grids. Finally, for grids with spatially varying grid ratio (and/or pitch) the images of Fig. 9 illustrate not only where in the image scatter is highest but also how the various scatter components (and angle of incidence) vary across the projection.

As acknowledged in Sec. II.B, the current work did not include bowtie filters in the simulation, which are in themselves a subject of research and are likely to be of greater benefit in some configurations than others. Other authors have shown that for some configurations, bowties are beneficial in terms of SPR reduction and image uniformity.[43,47,54,60] Bowties were omitted from the current study because they are not commonly used in all configurations studied here, to avoid further increasing the already large parameter space, and to maintain the focus of the current work on effects of system geometry in and of itself. Similarly, the simulations did not account for the effects of finite focal spot size. In particular, there is a trade-off between scatter reduction due to extended air gap and the associated increase in focal spot blur due to larger magnification.[18,71] Recognizing the importance of this trade-off in system design, the current study focused on specific CBCT configurations where system geometry has already been established—likely by a combination of such image quality considerations with mechanical/logistical constraints of the application.

The results presented here corroborate a variety of findings from previously reported experimental and simulation studies of individual configurations. For small animal systems, Colijn *et al.*[42] used MC methods to investigate a system with similar ADD to that assumed above (51 mm). Their results indicated SPR of 0.2–0.35 for water phantoms (60 mm diameter) and a realistic rat phantom, and a cupping level of 10%–15%, whereas we found SPR of 0.35 for a rat phantom and a cupping of 20%. While direct comparison is not possible due to differences in x-ray spectra (100 kVp in Ref. 42 vs 60 kVp in this work) and size of the objects, both studies indicate that scatter is a significant issue in small animal imaging, despite the small size of the typical subjects. This is most directly attributable to short air gaps employed in SA CBCT to accommodate relatively small field of view CCD sensors and low power sources. The MSK extremities CBCT configuration is another example of a compact geometry with short object-detector distance, so chosen to allow weight-bearing imaging in a natural standing stance.[3] Results indicate that extremities CBCT is likely to benefit from the incorporation of a grid, which provides a >50% reduction in cupping and SPR, and improves CNR over a grid-less acquisition without increase in dose. This is in agreement with earlier experimental studies[3] that showed antiscatter grids to yield ~20% improvement in soft-tissue CNR and 50% reduction in cupping in cylindrical phantoms and cadaveric knees. Compared to other compact CBCT configurations, the Breast geometry is characterized by an extended ADD of 32 cm and provides a more favorable geometry for scatter management. As shown in Fig. 4, this ADD corresponds to the transition between the region of steep SPR reduction and the region of more modest gains from further increases in air gap. We found SPR ~0.5 for a cylindrical 14 cm phantom and for a realistic breast phantom. CNR decreased with application of a grid despite a 50% reduction in SPR and a 5%–10% increase in contrast. This is similar to the experimental results of Kwan *et al.*,[43] who found SPR of 0.5, and twofold reduction in SPR and 18% increase in contrast with a 10:1 grid, but concluded that grids were not beneficial for their system due to their low (56.5%) primary transmission. Further increase in ADD by 10 cm was not found to significantly reduce SPR for a 14 cm breast, consistent with our finding that the benefits of extended ADD level off at approximately 30–50 cm for a 16 cm cylindrical phantom. Kwan *et al.*[43] further indicated that a bowtie can be beneficial for scatter mitigation but was not been considered in the study described above. Interventional C-arms provide even longer ADD than the Breast configuration (60 cm vs 32 cm). The results show the C-arm configuration to exhibit similar SPR, cupping, and contrast as breast CBCT, with grids again showing no benefit in CNR at constant dose, despite the reduction of artifacts. This is consistent with experimental results of Schafer *et al.*,[44] who showed a ~2-fold improvement in HU accuracy with a grid, accompanied however by a loss of soft-tissue CNR (reaching up to ~40% for a 10:1 grid, depending of the tissue type) and concluded that grids were not beneficial in this configuration. In Kyriakou and Kalender[45] experimental and MC studies of scatter in C-arm CBCT were also reported, showing SPR ~0.5 for a 16 cm PMMA cylinder at 60 cm object-detector distance, and demonstrating the efficacy of increased air gap in scatter reduction (almost 50% reduction in SPR for air gap increase from 4 cm to 30 cm), in

agreement with the results above. Reduction in SPR and image artifacts with a grid was also shown, but it was concluded that for objects smaller than approx. 16 cm, an increase in dose is needed to maintain the signal-to-noise ratio obtained by a gridless configuration. This agrees with the results of Fig. 6, where grids are shown to improve CNR for C-arm CBCT only for high SPRs. Finally, the Linac CBCT configuration represents a case with a relatively long air gap (ADD = 50 cm) but large body sites likely to generate a high scatter fraction. This is reflected in our finding of high SPR (>2.5) and strong cupping (∼20%) for the 28 cm Common Phantom. Grids clearly improve image uniformity and contrast for this embodiment, and the results indicate that they may be beneficial to CNR under conditions of high SPR corresponding to a ∼30 cm diameter object. This is similar to the MC results of Lazos and Williamson,[47] where SPR in excess of 2 was shown for some locations behind a pelvis, and a small improvement in CNR (10%–20%) at fixed dose was reported for pelvic imaging with a grid. Siewerdsen *et al.*[46] also showed significant reduction in image artifacts and improvement in contrast when a grid was incorporated in the Linac CBCT configuration but found that the potential benefit of grids in terms of CNR per unit square root dose should consider the tradeoffs among noise and spatial resolution in determining whether a grid was beneficial for a particular imaging task. This result hints at the complexities of assessing the true benefit of antiscatter grids versus a number of other imaging parameters such as spatial resolution, dose, and the imaging task that are somewhat beyond the simple metric of CNR utilized in the current work.

One limitation of the current study is its reliance on the independent atom approximation (IAA) in modeling the Rayleigh scattering process. IAA is commonly assumed in MC simulations of x-ray transport, but it neglects interference effects in the Rayleigh form factor,[72] which can lead to overestimation of the intensity of coherent scatter, especially at lower x-ray energies.[73–75] To obtain initial insight into the possible effect of such IAA bias on our results, a series of preliminary simulations was carried out. The interference effects were included in the Rayleigh form factor following Refs. 73 and 76, and a single projection of the Common Phantom was simulated for all embodiments with $5 \times 10^7$ photons. The root-mean-square errors due to neglecting interference were computed for all non-zero detector pixels in the Rayleigh scatter distributions and were found to be ∼5%–11% across all CBCT configurations without a grid. The errors in Rayleigh scatter estimation increased with a grid, reaching ∼25% for the lowest-energy spectrum (SA) and were ∼13%–20% for configurations utilizing a higher-energy beam. Future work (here and throughout the field of MC scatter modeling) will include alternative forms of coherent scatter interference models and validation of their influence on MC estimates of x-ray scatter distributions.

While the topic of scatter and scatter mitigation in CBCT has been well studied, such studies usually focus on a specific application and system geometry. The current work adds to such understanding by presenting a unified, accelerated Monte Carlo framework to provide a systematic, comparative analysis of scatter effects across a broad range of clinically relevant geometries and CBCT applications. The work demonstrates that not all CBCT geometries are equally burdened by x-ray scatter or equally benefit by incorporation of an antiscatter grid. In particular, the results reinforce the observation that maintaining a relatively long ADD is the best primary defense against scatter when permitted by clinical constraints, the desired scanner footprint, source power, and considerations of spatial resolution. For some CBCT configurations and imaging tasks, geometry alone may provide sufficient scatter reduction to obviate the need for any additional mechanisms for scatter rejection or algorithmic correction; in fact, scatter rejection by means of a grid may be detrimental to CNR at fixed dose in the embodiments characterized by longer air gaps. Even when grids are employed, there may be a need for additional software correction of the remaining scatter, especially in applications relying on quantitative accuracy in HU for purposes of dose calculation or quantitative CT. Such correction methods should account for the often highly heterogeneous scatter distributions in the presence of antiscatter grids.

## ACKNOWLEDGMENTS

The authors thank Yoshito Otake, Ph. D. (Johns Hopkins University) for assistance with GPU cone-beam reconstruction, and John Boone, Ph. D. (University of California Davis) for providing the digital breast phantom. The research was supported by academic-industry partnership with Carestream Health Inc. (Rochester, NY) and National Institutes of Health (NIH) Grant No. 2R01-CA-112163. A. Sisniega is supported by FPU grant (Spanish Ministry of Education), AMIT project, RECAVA-RETIC Network, Project Nos. TEC2010-21619-C04-01, TEC2011-28972-C02-01, and PI11/00616 (Spanish Ministry of Science and Education), ARTEMIS program (Comunidad de Madrid), and PreDiCT-TB partnership.

[a]Author to whom correspondence should be addressed. Electronic mail: wzbijewski@jhu.edu

[1]A. Sasov, "Ultra-fast micro-CT for in-vivo small animal imaging and industrial applications," Proc. SPIE **5535**, 733–739 (2004).
[2]J. J. Vaquero, S. Redondo, E. Lage, M. Abella, A. Sisniega, G. Tapias, M. L. S. Montenegro, and M. Desco, "Assessment of a new high-performance small-animal x-ray tomograph," IEEE Trans. Nucl. Sci. **55**, 898–905 (2008).
[3]W. Zbijewski, P. De Jean, P. Prakash, Y. Ding, J. W. Stayman, N. Packard, R. Senn, D. Yang, J. Yorkston, A. Machado, J. A. Carrino, and J. H. Siewerdsen, "A dedicated cone-beam CT system for musculoskeletal extremities imaging: design, optimization, and initial performance characterization," Med. Phys. **38**, 4700–4713 (2011).
[4]S. K. Koskinen, V. V. Haapamaki, J. Salo, N. C. Lindfors, M. Kortesniemi, L. Seppala, and K. T. Mattila, "CT arthrography of the wrist using a novel, mobile, dedicated extremity cone-beam CT (CBCT)," Skeletal Radiol. **42**(5), 649–657 (2012).
[5]R. A. Zoumalan, R. A. Lebowitz, E. Wang, K. Yung, J. S. Babb, and J. B. Jacobs, "Flat panel cone beam computed tomography of the sinuses," Otolaryngol. -Head Neck Surg. **140**, 841–844 (2009).
[6]J. Xu, D. D. Reh, J. P. Carey, M. Mahesh, and J. H. Siewerdsen, "Technical assessment of a cone-beam CT scanner for otolaryngology imaging: Image quality, dose, and technique protocols," Med. Phys. **39**, 4932–4942 (2012).
[7]L. Yu, T. J. Vrieze, M. R. Bruesewitz, J. M. Kofler, D. R. DeLone, J. F. Pallanch, E. P. Lindell, and C. H. McCollough, "Dose and image quality

evaluation of a dedicated cone-beam ct system for high-contrast neurologic applications," Am. J. Roentgenol. **194**, W193–W201 (2010).
[8]J. M. Boone, T. R. Nelson, K. K. Lindfors, and J. A. Seibert, "Dedicated breast CT: Radiation dose and image quality evaluation," Radiology **221**, 657–667 (2001).
[9]W. T. Yang, S. Carkaci, L. Chen, C. J. Lai, A. Sahin, G. J. Whitman, and C. C. Shaw, "Dedicated cone-beam breast CT: Feasibility study with surgical mastectomy specimens," Am. J. Roentgenol. **189**, 1312–1315 (2007).
[10]R. Fahrig, R. Dixon, T. Payne, R. L. Morin, A. Ganguly, and N. Strobel, "Dose and image quality for a cone-beam C-arm CT system," Med. Phys. **33**, 4541–4550 (2006).
[11]W. Kalender and Y. Kyriakou, "Flat-detector computed tomography (FD-CT)," Eur. Radiol. **17**, 2767–2779 (2007).
[12]J. H. Siewerdsen, D. J. Moseley, S. Burch, S. K. Bisland, A. Bogaards, B. C. Wilson, and D. A. Jaffray, "Volume CT with a flat-panel detector on a mobile, isocentric C-arm: Preclinical investigation in guidance of minimally invasive surgery," Med. Phys. **32**, 241–254 (2005).
[13]D. A. Jaffray, J. H. Siewerdsen, J. W. Wong, and A. A. Martinez, "Flat-panel cone-beam computed tomography for image-guided radiation therapy," Int. J. Radiat. Oncol., Biol., Phys. **53**, 1337–1349 (2002).
[14]I. S. Grills, G. Hugo, L. L. Kestfn, A. P. Galerani, K. K. Chao, J. Wloch, and D. Yan, "Image-guided radiotherapy via daily online cone-beam CT substantially reduces margin requirements for stereotactic lung radiotherapy," Int. J. Radiat. Oncol., Biol., Phys. **70**, 1045–1056 (2008).
[15]P. C. Johns and M. Yaffe, "Scattered radiation in fan beam imaging-systems," Med. Phys. **9**, 231–239 (1982).
[16]G. H. Glover, "Compton scatter effects in CT reconstructions," Med. Phys. **9**, 860–867 (1982).
[17]M. Endo, T. Tsunoo, N. Nakamori, and K. Yoshida, "Effect of scattered radiation on image noise in cone beam CT," Med. Phys. **28**, 469–474 (2001).
[18]I. S. Kyprianou, S. Rudin, D. R. Bednarek, and K. R. Hoffmann, "Generalizing the MTF and DQE to include x-ray scatter and focal spot unsharpness: Application to a new microangiographic system," Med. Phys. **32**, 613–626 (2005).
[19]P. M. Joseph and R. D. Spital, "The effects of scatter in x-ray computed-tomography," Med. Phys. **9**, 464–472 (1982).
[20]R. Ning, X. Y. Tang, and D. Conover, "X-ray scatter correction algorithm for cone beam CT imaging," Med. Phys. **31**, 1195–1202 (2004).
[21]X. Liu, C. Shaw, M. Altunbas, and T. Wang, "A scanning sampled measurement (SSM) technique for scatter measurement and correction in cone beam breast CT," Med. Phys. **32**, 2093–2093 (2005).
[22]L. Zhu, N. Strobel, and R. Fahrig, "X-ray scatter correction for cone-beam CT using moving blocker array," Proc. SPIE **5745**, 251–258 (2005).
[23]L. Zhu, Y. Q. Xie, J. Wang, and L. Xing, "Scatter correction for cone-beam CT in radiation therapy," Med. Phys. **36**, 2258–2268 (2009).
[24]J. H. Siewerdsen, M. J. Daly, B. Bakhtiar, D. J. Moseley, S. Richard, H. Keller, and D. A. Jaffray, "A simple, direct method for x-ray scatter estimation and correction in digital radiography and cone-beam CT," Med. Phys. **33**, 187–197 (2006).
[25]L. Zhu, N. R. Bennett, and R. Fahrig, "Scatter correction method for x-ray CT using primary modulation: Theory and preliminary results," IEEE Trans. Med. Imaging **25**, 1573–1587 (2006).
[26]K. Yang, G. Burkett, and J. M. Boone, "An object-specific and dose-sparing scatter correction approach for a dedicated cone-beam breast CT system using a parallel-hole collimator," Proc. SPIE **8313**, 831303-1–831303-6 (2012).
[27]M. Bertram, J. Wiegert, and G. Rose, "Potential of software-based scatter corrections in cone-beam volume CT," Proc. SPIE **5745**, 259–270 (2005).
[28]L. A. Love and R. A. Kruger, "Scatter estimation for a digital radiographic system using convolution filtering," Med. Phys. **14**, 178–185 (1987).
[29]J. A. Seibert and J. M. Boone, "X-ray scatter removal by deconvolution," Med. Phys. **15**, 567–575 (1988).
[30]J. S. Maltz, B. Gangadharan, S. Bose, D. H. Hristov, B. A. Faddegon, A. Paidi, and A. R. Bani-Hashemi, "Algorithm for x-ray scatter, beam-hardening, and beam profile correction in diagnostic (kilovoltage) and treatment (Megavoltage) cone beam CT," IEEE Trans. Med. Imaging **27**, 1791–1810 (2008).
[31]M. Sun and J. M. Star-Lack, "Improved scatter correction using adaptive scatter kernel superposition," Phys. Med. Biol. **55**, 6695–6720 (2010).
[32]G. Jarry, S. A. Graham, D. J. Moseley, D. J. Jaffray, J. H. Siewerdsen, and F. Verhaegen, "Characterization of scattered radiation in kV CBCT images using Monte Carlo simulations," Med. Phys. **33**, 4320–4329 (2006).
[33]E. Mainegra-Hing and I. Kawrakow, "Variance reduction techniques for fast Monte Carlo CBCT scatter correction calculations," Phys. Med. Biol. **55**, 4495–4507 (2010).
[34]A. P. Colijn and F. J. Beekman, "Accelerated simulation of cone beam x-ray scatter projections," IEEE Trans. Med. Imaging **23**, 584–590 (2004).
[35]G. Jarry, S. A. Graham, D. A. Jaffray, D. J. Moseley, and F. Verhaegen, "Scatter correction for kilovoltage cone-beam computed tomography (CBCT) images using Monte Carlo simulations," Proc. SPIE **6142**, 614254 (2006).
[36]W. Zbijewski and F. J. Beekman, "Efficient Monte Carlo based scatter artifact reduction in cone-beam micro-CT," IEEE Trans. Med. Imaging. **25**, 817–827 (2006).
[37]G. Poludniowski, P. M. Evans, V. N. Hansen, and S. Webb, "An efficient Monte Carlo-based algorithm for scatter correction in keV cone-beam CT," Phys. Med. Biol. **54**, 3847–3864 (2009).
[38]G. Bootsma, F. Verhaegen, and D. Jaffray, "SU-F-BRCD-04: Efficient scatter distribution estimation and correction in CBCT using concurrent Monte Carlo fitting," Med. Phys. **39**, 3856 (2012).
[39]Y. Kyriakou, T. Riedel, and W. A. Kalender, "Combining deterministic and Monte Carlo calculations for fast estimation of scatter intensities in CT," Phys. Med. Biol. **51**, 4567–4586 (2006).
[40]A. Badal and A. Badano, "Accelerating Monte Carlo simulations of photon transport in a voxelized geometry using a massively parallel graphics processing unit," Med. Phys. **36**, 4878–4880 (2009).
[41]U. Neitzel, "Grids or air gaps for scatter reduction in digital radiography: A model calculation," Med. Phys. **19**, 475–481 (1992).
[42]A. P. Colijn, W. Zbijewski, A. Sasov, and F. J. Beekman, "Experimental validation of a rapid Monte Carlo based micro-CT simulator," Phys. Med. Biol. **49**, 4321–4333 (2004).
[43]A. L. Kwan, J. M. Boone, and N. Shah, "Evaluation of x-ray scatter properties in a dedicated cone-beam breast CT scanner," Med. Phys. **32**, 2967–2975 (2005).
[44]S. Schafer, J. W. Stayman, W. Zbijewski, C. Schmidgunst, G. Kleinszig, and J. H. Siewerdsen, "Antiscatter grids in mobile C-arm cone-beam CT: Effect on image quality and dose," Med. Phys. **39**, 153–159 (2012).
[45]Y. Kyriakou and W. Kalender, "Efficiency of antiscatter grids for flat-detector CT," Phys. Med. Biol. **52**, 6275–6293 (2007).
[46]J. H. Siewerdsen, D. J. Moseley, B. Bakhtiar, S. Richard, and D. A. Jaffray, "The influence of antiscatter grids on soft-tissue detectability in cone-beam computed tomography with flat-panel detectors," Med. Phys. **31**, 3506–3520 (2004).
[47]D. Lazos and J. F. Williamson, "Monte Carlo evaluation of scatter mitigation strategies in cone-beam CT," Med. Phys. **37**, 5456–5470 (2010).
[48]F. Salvat, J. M. Fernández-Varea, and J. Sempau, "PENELOPE - Code System for Monte Carlo Simulation of Electron and Photon Transport," Nuclear Energy Agency OECD (Issy-les-Moulineaux), 2006.
[49]J. H. Siewerdsen, A. M. Waese, D. J. Moseley, S. Richard, and D. A. Jaffray, "Spektr: A computational tool for x-ray spectral analysis and imaging system optimization," Med. Phys. **31**, 3057–3067 (2004).
[50]J. M. Boone and J. A. Seibert, "An accurate method for computer-generating tungsten anode x-ray spectra from 30 to 140 kV," Med. Phys. **24**, 1661–1670 (1997).
[51]A. J. Walker, "An efficient method for generating discrete random variable with general distributions," ACM Trans. Math. Softw. **3**, 253–256 (1977).
[52]E. Woodcock, T. Murphy, P. Hemmings, and T. Longworth, "Techniques used in the GEM code for Monte Carlo neutronics calculations in reactors and other systems of complex geometry," *Proc. Conference on the Application of Computing Methods to Reactor Problems*, ANL-7050, 557–579 (1965).
[53]M. H. Kalos, "On estimation of flux at a point by Monte Carlo," Nucl. Sci. Eng. **16**, 111–117 (1963).
[54]J. F. Williamson, "Monte Carlo evaluation of kerma at a point for photon transport problems," Med. Phys. **14**, 567–576 (1987).
[55]R. L. Siddon, "Fast calculation of the exact radiological path for a three-dimensional CT array," Med. Phys. **12**, 252–255 (1985).
[56]G. J. Day and D. R. Dance, "X-ray transmission formula for antiscatter grids," Phys. Med. Biol. **28**, 1429–1433 (1983).
[57]S. Richard, J. H. Siewerdsen, D. A. Jaffray, D. J. Moseley, and B. Bakhtiar, "Generalized DQE analysis of radiographic and dual-energy imaging using flat-panel detectors," Med. Phys. **32**, 1397–1413 (2005).
[58]J. A. Rowlands and K. W. Taylor, "Absorption and noise in cesium iodide x-ray image intensifiers," Med. Phys. **10**, 786–795 (1983).

[59]A. L. Kwan, J. M. Boone, K. Yang, and S. Y. Huang, "Evaluation of the spatial resolution characteristics of a cone-beam breast CT scanner," Med. Phys. **34**, 275–281 (2007).
[60]N. Mail, D. J. Moseley, J. H. Siewerdsen, and D. A. Jaffray, "The influence of bowtie filtration on cone-beam CT image quality," Med. Phys. **36**, 22–32 (2009).
[61]H. Q. Woodard and D. R. White, "The composition of body-tissues," Br. J. Radiol. **59**, 1209–1219 (1986).
[62]B. Dogdas, D. Stout, A. F. Chatziioannou, and R. M. Leahy, "Digimouse: A 3D whole body mouse atlas from CT and cryosection data," Phys. Med. Biol. **52**, 577–587 (2007).
[63]S. X. Gu, R. Gupta, and I. Kyprianou, "Computational high-resolution heart phantoms for medical imaging and dosimetry simulations," Phys. Med. Biol. **56**, 5845–5864 (2011).
[64]www.itis.ethz.ch. Last accessed Februrary 2013.
[65]N. D. Prionas, G. W. Burkett, S. E. McKenney, L. Chen, R. L. Stern, and J. M. Boone, "Development of a patient-specific two-compartment anthropomorphic breast phantom," Phys. Med. Biol. **57**, 4293–4307 (2012).
[66]A. Badal and A. Badano, "SU-E-I-68: Fast and accurate estimation of organ doses in medical imaging using a GPU-accelerated Monte Carlo simulation code," Med. Phys. **38**, 3411 (2011).
[67]W. Zbijewski, A. Sisniega, J. J. Vaquero, A. Muhit, N. Packard, R. Senn, D. Yang, J. Yorkston, J. A. Carrino, and J. H. Siewerdsen, "Dose and scatter characteristics of a novel cone beam CT system for musculoskeletal extremities," Proc. SPIE **8313**, 831318 (2012).
[68]L. A. Feldkamp, L. C. Davis, and J. W. Kress, "Practical cone-beam algorithm," J. Opt. Soc. Am. A **1**, 612–619 (1984).
[69]J. H. Siewerdsen and D. A. Jaffray, "Cone-beam computed tomography with a flat-panel imager: magnitude and effects of x-ray scatter," Med. Phys. **28**, 220–231 (2001).
[70]H. H. Barrett, S. K. Gordon, and R. S. Hershel, "Statistical limitations in transaxial tomography," Comput. Biol. Med. **6**, 307–323 (1976).
[71]J. H. Siewerdsen and D. A. Jaffray, "Optimization of x-ray imaging geometry (with specific application to flat-panel cone-beam computed tomography)," Med. Phys. **27**, 1903–1914 (2000).
[72]P. C. Johns and M. J. Yaffe, "Coherent scatter in diagnostic radiology," Med. Phys. **10**, 40–50 (1983).
[73]G. Poludniowski, P. M. Evans, and S. Webb, "Rayleigh scatter in kilovoltage x-ray imaging: Is the independent atom approximation good enough?," Phys. Med. Biol. **54**, 6931–6942 (2009).
[74]D. M. Cunha, A. Tomal, and M. E. Poletti, "Evaluation of scatter-to-primary ratio, grid performance and normalized average glandular dose in mammography by Monte Carlo simulation including interference and energy broadening effects," Phys. Med. Biol. **55**, 4335–4359 (2010).
[75]C. J. Leliveld, J. G. Maas, V. R. Bom, and C. W. E. van Eijk, "Monte Carlo modeling of coherent scattering: Influence of interference," IEEE Trans. Nucl. Sci. **43**, 3315–3321 (1996).
[76]A. Tartari, A. Taibi, C. Bonifazzi, and C. Baraldi, "Updating of form factor tabulations for coherent scattering of photons in tissues," Phys. Med. Biol. **47**, 163–175 (2002).